

Feedback Control for Multi-Objective Graph Self-Supervision

Karish Grover^{1,2} Theodore Vasiloudis³ Han Xie³ Sixing Lu³ Xiang Song³ Christos Faloutsos¹

Abstract

Can multi-task self-supervised learning on graphs be coordinated without the usual tug-of-war between objectives? Graph self-supervised learning (SSL) offers a growing toolbox of pretext objectives—mutual information, reconstruction, contrastive learning—yet combining them reliably remains a challenge due to objective interference and training instability. Most multi-pretext pipelines use *per-update mixing*, forcing every parameter update to be a compromise, leading to three failure modes: *Disagreement* (conflict-induced negative transfer), *Drift* (nonstationary objective utility), and *Drought* (hidden starvation of underserved objectives). We argue that coordination is fundamentally a *temporal allocation* problem: deciding *when* each objective receives optimization budget, not merely how to weigh them. We introduce `ControlG`, a control-theoretic framework that recasts multi-objective graph SSL as *feedback-controlled temporal allocation* by estimating per-objective difficulty and pairwise antagonism, planning target budgets via a Pareto-aware log-hypervolume planner, and scheduling with a Proportional–Integral–Derivative (PID) controller. Across 9 datasets, `ControlG` consistently outperforms state-of-the-art baselines, while producing an auditable schedule that reveals *which objectives drove learning*.

1. Introduction

Self-supervised pretraining has become a default route to transferable representations when labels are scarce, and graphs are no exception. Graph SSL has produced a diverse toolbox of objectives encoding different inductive biases: mutual-information maximization (Veličković et al., 2018), contrastive learning under augmentations (You et al., 2020; Zhu et al., 2020), negative-free bootstrapping (Thakoor

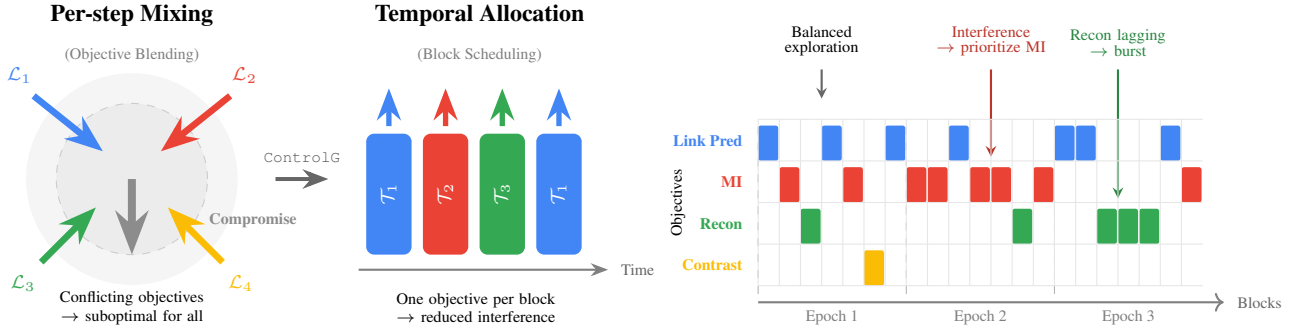
¹Carnegie Mellon University ²The work was done during Karish Grover’s internship at Amazon, US. ³Amazon. Correspondence to: Karish Grover <karishg@cs.cmu.edu>.

et al., 2021), and masked reconstruction (Hou et al., 2022). Yet *which* objective works best depends heavily on the dataset, downstream task, and training stage—motivating multi-pretext approaches that combine or search over objectives (Jin et al., 2021).

A natural response is to train with multiple pretext objectives jointly, hoping that the encoder absorbs a richer set of signals. Many multi-pretext and multi-task recipes operationalize this by optimizing a weighted sum of losses or by combining gradients into a single update direction at every step. In graph SSL specifically, ParetoGNN (Ju et al., 2022) uses multi-gradient descent (MGDA) (Sener & Koltun, 2018) to reconcile multiple pretext tasks, and WAS (Fan et al., 2024) proposes an instance-level framework that decouples selecting and weighing tasks. In general multi-task learning, a large body of work designs per-step scalarization rules using MGDA or mitigates interference through gradient manipulation (Yu et al., 2020; Liu et al., 2021). These approaches are effective in many settings, but they still share a core actuation pattern: each training step blends signals across objectives in parameter space, implicitly assuming that an appropriate instantaneous compromise can be found and maintained.

Research gaps in multi-objective graph SSL. When objectives are self-supervised pretext tasks, training exhibits three recurring failure modes. **(a) Drift:** the utility of a pretext objective is nonstationary—an objective that accelerates learning early can become redundant later—so fixed or weakly adaptive weights lag behind regime changes (Guo et al., 2018a). **(b) Disagreement:** objectives frequently induce conflicting gradient directions, forcing a compromise that can be simultaneously suboptimal for all (Sener & Koltun, 2018; Yu et al., 2020; Liu et al., 2021). **(c) Drought:** adaptive weighting can starve objectives by driving their weights toward zero, making it unclear whether an objective ever meaningfully shaped the representation. Together, these issues make multi-pretext training brittle: current systems are largely *open-loop*, specifying a mixing rule and hoping the dynamics remain well-behaved.

Key idea. Instead of blending all self-supervised objectives at every step, train one objective at a time using feedback control to schedule and adapt.



(a) The core insight. Per-step gradient mixing forces compromise when objectives conflict. ControlG separates objectives in time, giving each dedicated compute blocks—eliminating instantaneous interference.

Figure 1. Motivation and overview of ControlG. **(a)** The key insight: temporal allocation avoids objective conflict by dedicating one objective per block. **(b)** The learned schedule is interpretable and auditable—the planner adapts allocation based on interference and demand signals.

ControlG addresses these gaps by coordinating objectives through *temporal allocation* under a fixed compute budget. At a slower sensing timescale, it performs *state estimation on the full graph* to obtain two signals per objective: (i) a *spectral demand* indicator that measures how rapidly the objective’s learning signal varies over the graph and is motivated by the spectral/low-pass view of message passing (Nt & Maehara, 2019) (e.g., simplified GCN propagation corresponds to a fixed low-pass filter); and (ii) an *interference* indicator derived from local multi-objective gradient geometry, where MGDA provides Pareto-relevant weights for which objectives are actively constraining the trade-off at the current iterate. Based on these state estimates, a *Pareto-aware planner* produces a target allocation using log-hypervolume sensitivities, leveraging the hypervolume indicator’s standard role as a Pareto-compliant scalarization (Guerreiro et al., 2020). Finally, a *tracking controller* converts the continuous allocation target into discrete task choices by tracking allocation deficits with a PID-style feedback law; this deficit perspective is closely related to classic deficit-counter scheduling ideas (e.g., deficit round robin (Shreedhar & Varghese, 1996)), which ensure long-run fairness when service is indivisible. The end result is an interpretable, auditable training process: the planner explains *why* an objective should receive budget (priority + state), and the controller ensures it actually receives that budget over time. We hereby summarize our contributions:

- We introduce ControlG, a closed-loop control framework for coordinating multiple graph SSL pretext objectives via sensing, Pareto-aware planning, and feedback-based execution. To the best of our knowledge, this is the first work to cast multi-objective graph SSL coordination as a *closed-loop scheduling problem with explicit allocation tracking*, using deficit-based

feedback control to execute discrete single-objective blocks rather than per-step loss weighting.

- We propose full-graph state estimation signals that quantify objective demand and objective interference, enabling principled adaptation to nonstationarity (drift) and gradient conflicts (disagreement) without collapsing all objectives into a single per-step compromise.
- We develop a Pareto-aware planner based on log-hypervolume sensitivities and a deficit-tracking PID controller that executes discrete single-task blocks while explicitly mitigating starvation (drought).
- We empirically evaluate ControlG against strong single-objective and multi-pretext baselines on standard graph SSL benchmarks (Sec. 5), showing improved robustness and transfer.

2. Related Work

Graph SSL and multi-pretext integration. Graph SSL has produced diverse pretext objectives: contrastive methods like DGI (Veličković et al., 2018), GraphCL (You et al., 2020), and GCA (Zhu et al., 2021); bootstrapping approaches like BGRL (Thakoor et al., 2021); and reconstruction objectives like GraphMAE (Hou et al., 2022). Since no single objective dominates across graphs (Liu et al., 2022; Ju et al., 2024), recent work integrates multiple objectives. AUTOSSL (Jin et al., 2021) searches task combinations via label-free surrogates but uses static weights once selected, limiting adaptivity to training dynamics. PARETOGNN (Ju et al., 2022) applies multi-objective gradient updates for Pareto efficiency, yet per-step mixing can force compromise when objectives conflict and provides no explicit coverage accounting. WAS (Fan et al., 2024) decouples selection

and weighting at the instance level but still blends all objectives per update. GraphTCM (Fang et al., 2024) models task correlations, confirming they vary across datasets—motivating our adaptive, feedback-driven approach. Unlike these methods, ControlG coordinates via *temporal allocation*: time-sharing single-task blocks with explicit deficit tracking, avoiding forced compromise while ensuring auditable coverage.

Multi-objective optimization and MTL. Gradient-based MTL methods design per-step update rules: MGDA finds minimum-norm gradient combinations (Sener & Koltun, 2018), PCGrad/CAGrad reduce interference (Yu et al., 2020; Liu et al., 2021), and Nash-MTL uses bargaining (Navon et al., 2022). Imbalance-focused approaches include GradNorm (Chen et al., 2018) and uncertainty weighting (Kendall et al., 2018). These methods address conflict through instantaneous scalarization but still produce a single update direction, making it difficult to separate objectives in time or provide block-level coverage accountability. ControlG instead uses gradient geometry for *sensing* (interference feedback) while actuating through time-sharing.

Task scheduling and curricula. Dynamic Task Prioritization (Guo et al., 2018b) and AdaTask (Laforgue et al., 2022) adapt *when* to train tasks, but are not developed for graph SSL and lack Pareto-aware planning. Without explicit allocation tracking, schedules can still exhibit hidden starvation. ControlG combines a Pareto-aware planner with deficit-tracking control, yielding interpretable time-sharing with coverage guarantees.

3. Background and Preliminaries

We fix notation and recall the primitives ControlG builds on: multi-objective gradient geometry, spectral smoothness, hypervolume-based scalarization, and PID control.

Setup and notation. Let $G = (V, E, \mathbf{X})$ be an attributed graph with $n = |V|$ nodes, adjacency $\mathbf{A} \in \{0, 1\}^{n \times n}$, degree matrix $\mathbf{D} = \text{diag}(d_1, \dots, d_n)$, and node features $\mathbf{X} \in \mathbb{R}^{n \times d}$. A graph encoder f_θ produces embeddings $\mathbf{Z} = f_\theta(G) \in \mathbb{R}^{n \times h}$. We consider K pretext tasks $\{\mathcal{T}_k\}_{k=1}^K$ with losses $\{\mathcal{L}_k(\theta)\}_{k=1}^K$, treating training as minimizing the vector objective $\mathcal{L}(\theta) = (\mathcal{L}_1, \dots, \mathcal{L}_K) \in \mathbb{R}^K$.

Pareto optimality and MGDA. A point θ *Pareto-dominates* θ' if $\mathcal{L}_k(\theta) \leq \mathcal{L}_k(\theta')$ for all k with strict inequality for at least one; a point is *Pareto-optimal* if undominated. *Pareto stationarity*—a first-order necessary condition—holds when $\exists \lambda \in \Delta^K$ s.t. $\sum_k \lambda_k \nabla_\theta \mathcal{L}_k = \mathbf{0}$, where Δ^K is the probability simplex. Intuitively, no direction simultaneously decreases all objectives.

The multi-gradient descent algorithm (MGDA) finds the minimum-norm convex combination of gradients (Sener & Koltun, 2018):

$$\lambda^* \in \arg \min_{\lambda \in \Delta^K} \left\| \sum_{k=1}^K \lambda_k g_k \right\|_2^2, \quad g_k := \nabla_\theta \mathcal{L}_k. \quad (1)$$

When $\sum_k \lambda_k^* g_k \neq \mathbf{0}$, this yields a common descent direction that improves all objectives. We use MGDA weights λ^* as an interference signal: objectives with high weight are actively constraining the trade-off at the current iterate.

Spectral smoothness. We use the normalized Laplacian $\tilde{\mathbf{L}} := \mathbf{I} - \mathbf{D}^{-1/2} \mathbf{A} \mathbf{D}^{-1/2}$ to quantify signal smoothness on the graph. For a signal $\mathbf{H} \in \mathbb{R}^{n \times d}$, the Dirichlet energy $\mathcal{E}(\mathbf{H}) = \text{tr}(\mathbf{H}^\top \tilde{\mathbf{L}} \mathbf{H})$ measures variation across edges. Since this scales with $\|\mathbf{H}\|_F^2$, we use the Rayleigh quotient $\text{RQ}(\mathbf{H}) := \mathcal{E}(\mathbf{H}) / \|\mathbf{H}\|_F^2$, interpretable as average graph frequency (Von Luxburg, 2007). Because GNNs act as low-pass filters (Nt & Maehara, 2019), objectives inducing high-RQ signals are spectrally harder to optimize.

Dominated hypervolume. To scalarize multi-objective progress while remaining sensitive to trade-offs, we use the log-hypervolume indicator (Guerreiro et al., 2020). For a reference point $\mathbf{r} \in \mathbb{R}^K$ with $r_k > \mathcal{L}_k$ (worse than current values), $\log \mathcal{H} = \sum_k \log(r_k - \mathcal{L}_k)$ decomposes additively and is numerically stable. The gradient $\partial \log \mathcal{H} / \partial \mathcal{L}_k = -1/(r_k - \mathcal{L}_k)$ shows that proximity to the reference amplifies sensitivity, naturally prioritizing lagging objectives.

PID control and deficit tracking. We track target allocations via discrete-time PID control. Let $e_k(m) = N_k^{\text{ref}}(m) - N_k(m)$ be the deficit (target minus actual count) for task k at block m . The controller output is:

$$\nu_k(m) = K_P e_k(m) + K_I \sum_{\tau \leq m} e_k(\tau) + K_D \Delta e_k(m),$$

where $\Delta e_k(m) = e_k(m) - e_k(m-1)$. We map $\nu(m)$ to probabilities via softmax. This deficit-tracking view parallels deficit round robin scheduling (Shreedhar & Varghese, 1996), which accumulates “service credit” to ensure long-run fairness when service is discrete.

4. ControlG: Overview

The core idea behind ControlG is to replace per-step objective blending with *temporal allocation*: rather than forcing every parameter update to compromise across all objectives, we dedicate consecutive optimization steps to a single objective at a time and use feedback control to decide which objective to train next. This reframes multi-objective coordination as a closed-loop scheduling problem, where the learning system repeatedly (i) *senses* which objectives are currently difficult or mutually antagonistic for the

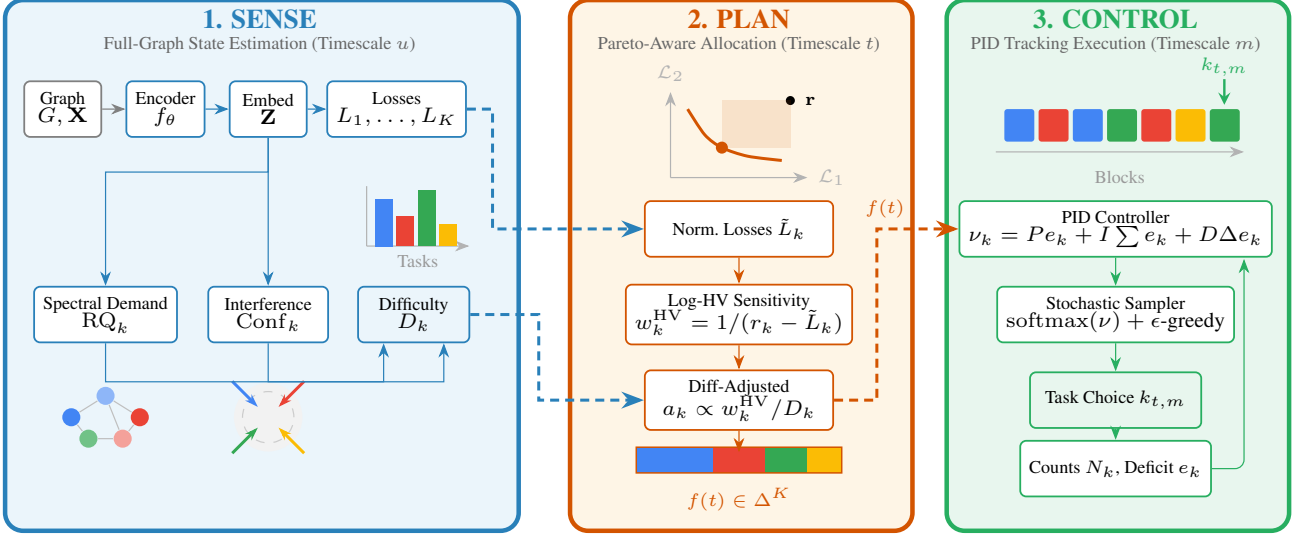


Figure 2. Overview of ControlG. The framework decomposes multi-task graph self-supervised learning into three coupled loops operating at different timescales. **(1) SENSE** (timescale u): A shared encoder f_θ maps the graph (G, \mathbf{X}) to embeddings \mathbf{Z} , from which per-task losses L_k are computed. State estimation derives two difficulty signals—*Spectral Demand* (RQ_k), measuring how high-frequency the learning signal is on the graph, and *Interference* ($Conf_k$), measuring gradient conflicts with other Pareto-relevant objectives—which are combined into a composite difficulty state D_k . **(2) PLAN** (timescale t): Normalized losses \tilde{L}_k are converted to *Log-HV sensitivities* $w_k^{HV} = 1/(r_k - \tilde{L}_k)$, quantifying each objective’s marginal contribution to Pareto progress. These are tempered by difficulty to produce a *difficulty-adjusted allocation* $a_k \propto w_k^{HV} / D_k$, normalized to an epoch-level target $f(t) \in \Delta^K$. **(3) CONTROL** (timescale m): A PID controller tracks the allocation plan by computing logits ν_k from deficits $e_k = N_k^{\text{ref}} - N_k$, their integral, and derivative. A stochastic sampler (softmax with ϵ -greedy exploration) selects the task $k_{t,m}$ for each block, updating counts N_k and closing the feedback loop. Dashed arrows indicate cross-module information flow.

shared encoder, (ii) *plans* an explicit target allocation over objectives using a Pareto-monotone progress surrogate, and (iii) *tracks* that plan with a lightweight controller. Figure 2 illustrates this three-loop architecture. The time-sharing view exposes allocation and ordering as first-class degrees of freedom, yields interpretable schedules, and keeps the inner-loop optimizer unchanged.

Formally, let $\{L_k(\theta)\}_{k=1}^K$ be SSL objectives sharing encoder parameters θ . Training is organized into epochs $t \in \{1, \dots, T\}$, each containing B_{ep} mini-batches. We group consecutive mini-batches into *blocks* of size B_{block} , yielding $M := \lceil B_{\text{ep}} / B_{\text{block}} \rceil$ blocks per epoch, indexed by $m \in \{1, \dots, M\}$. At block (t, m) the scheduler selects a task index $k_{t,m} \in \{1, \dots, K\}$ and performs B_{block} standard optimizer steps on that task only,

$$\text{for } j = 1, \dots, B_{\text{block}} : \quad \theta \leftarrow \theta - \eta \nabla_\theta L_{k_{t,m}}(\theta; \xi_{t,m,j}), \quad (2)$$

where $\xi_{t,m,j}$ denotes the randomness in sampling/augmentations for the j -th mini-batch inside the block. The key question is therefore not how to combine objectives within a step, but how to select the sequence $\{k_{t,m}\}$ so that progress across objectives is balanced and robust. We answer this by maintaining a compact per-task state computed on the full training graph (Sec. 4.1), converting that state into an allocation target $f(t) \in \Delta^K$

(Sec. 4.2), and tracking $f(t)$ through a deficit-based controller (Sec. 4.3).

4.1. State Estimation on the Full Graph

ControlG maintains a compact per-objective state that is updated every u blocks and consumed by the planner (Sec. 4.2) and controller (Sec. 4.3). State estimation is performed on the *full training graph* $G = (V, E)$ so that the signals correspond to the same global objectives being optimized. At each sensing step, for every objective $k \in \{1, \dots, K\}$ we estimate (i) a *spectral demand* score that captures how rapidly the objective’s learning signal varies over the graph, (ii) an *interference* score that captures conflicts with other objectives in parameter space, and (iii) a normalized loss \tilde{L}_k used for planning. We combine (i)–(ii) into a single bounded difficulty state D_k that tempers allocation decisions. All derivations and formal guarantees are provided in App. A.

4.1.1. SPECTRAL DEMAND FROM REPRESENTATION-GRADIENT VARIATION

To define a graph-frequency notion we require a node-indexed signal. Parameter gradients are not naturally node-indexed, so we use the objective’s gradient with respect to node embeddings. Let $z_v \in \mathbb{R}^h$ denote the embedding of

node $v \in V$, and for objective k define the *representation-gradient field* $h_k(v) := \nabla_{z_v} L_k \in \mathbb{R}^h$, stacking rows into $H_k \in \mathbb{R}^{n \times h}$. Let $\tilde{\mathbf{L}}$ be the symmetric normalized Laplacian.¹ The *Dirichlet energy* $\mathcal{E}_k := \text{tr}(H_k^\top \tilde{\mathbf{L}} H_k)$ measures edge-wise variation (App. A.2). Since \mathcal{E}_k scales with gradient magnitude, our spectral-demand state is the scale-invariant *Rayleigh quotient*

$$\text{RQ}_k(\theta) := \frac{\mathcal{E}_k(\theta)}{\|H_k\|_F^2 + \varepsilon}, \quad (3)$$

which, as shown in App. A.3, equals an energy-weighted average Laplacian eigenvalue of H_k ; larger RQ_k indicates that the learning signal concentrates on higher graph frequencies (sharper variation across edges). Why interpret RQ_k as a *difficulty proxy*? Many message-passing GNNs behave as low-pass graph filters (Nt & Maehara, 2019), attenuating higher-frequency components, which directly limits attainable progress:

Proposition 4.1 (Spectral demand bounds attainable progress; informal, see Prop. A.8 in App. A.4). *Assume representation updates act as a low-pass graph filter. Then, for fixed gradient energy $\|H_k\|_F^2$, the first-order loss decrease per update is upper-bounded by a quantity that is non-increasing in RQ_k .*

4.1.2. INTERFERENCE VIA PARETO-RELEVANT GRADIENT GEOMETRY

Spectral demand captures graph-structural difficulty but not conflicts from shared parameters. We therefore measure interference in parameter space. Let $g_k := \nabla_{\theta} L_k$ be the parameter gradient for objective k . A first-order expansion shows that a step on k increases L_j whenever $\langle g_j, g_k \rangle < 0$ (Claim A.10 in App. A.5), motivating negative cosine as a conflict indicator. To focus on Pareto-relevant objectives, we use MGDA as a *measurement oracle*. Because MGDA’s QP depends on gradient magnitudes, we first normalize each gradient to unit norm, $\hat{g}_k := g_k / \|g_k\|_2$, ensuring scale-invariance across objectives with different loss magnitudes. MGDA then solves

$$\lambda^* \in \arg \min_{\lambda \in \Delta^K} \left\| \sum_j \lambda_j \hat{g}_j \right\|^2,$$

returning weights that identify objectives locally constraining the Pareto compromise based on directional conflict rather than magnitude (App. A.5–A.6). With pairwise conflict $c_{k,j} := [-\cos(g_k, g_j)]_+$, we define interference as $\text{Conf}_k := \sum_{j \neq k} \lambda_j^* c_{k,j}$, which is large when k conflicts with several Pareto-relevant objectives.

¹ $\tilde{\mathbf{L}} = \mathbf{I} - \mathbf{D}^{-1/2} \mathbf{A} \mathbf{D}^{-1/2}$; for directed graphs we symmetrize the adjacency.

4.1.3. COMPOSITE DIFFICULTY STATE AND NORMALIZED LOSSES

Finally, we combine spectral demand and interference into a single bounded difficulty state. At each sensing step we robust-normalize RQ_k and Conf_k across objectives to obtain \bar{R}_k and \bar{C}_k , and update

$$s_k := (1-\rho) D_k + \rho (\alpha \bar{R}_k + \beta \bar{C}_k), \\ D_k \leftarrow \text{clip}(s_k, [D_{\min}, D_{\max}]), \quad (4)$$

where \bar{R}_k, \bar{C}_k denote the normalized scores. We use this linear combination as a monotone aggregator with interpretable coefficients; App. A.7 discusses alternatives. In parallel, we maintain a normalized loss state \tilde{L}_k for planning by smoothing with an EMA and dividing by a fixed scale, so the planner is invariant to loss units (see App. B).

4.2. STRATEGIC PLANNING: LOG-HYPERVOLUME ALLOCATION

The planner converts the state estimates from Sec. 4.1 into an epoch-level allocation target $f(t) \in \Delta^K$, where $f_k(t)$ is the desired fraction of blocks to devote to objective k during epoch t . We want a scalar progress signal that is *Pareto-compliant*: if all normalized losses weakly improve and at least one strictly improves (a strict Pareto improvement), the signal should strictly increase. A widely used Pareto-compliant choice is the dominated hypervolume (HV) relative to a reference point; in our setting we apply HV to the *singleton* loss vector $\bar{\ell}(t) = (\tilde{L}_1(t), \dots, \tilde{L}_K(t))$.

Singleton hypervolume and reference point. Let $\mathbf{r}(t) \in \mathbb{R}^K$ be a reference point such that $r_k(t) > \tilde{L}_k(t)$ for all k . For minimization, the dominated hypervolume of a single point reduces to the axis-aligned box volume $\text{HV}(t) := \prod_k (r_k(t) - \tilde{L}_k(t))$. We use its log for numerical stability and separable sensitivities:

$$\phi(t) := \log \text{HV}(t) = \sum_{k=1}^K \log (r_k(t) - \tilde{L}_k(t)). \quad (5)$$

All formal properties (Pareto compliance for fixed \mathbf{r} , reference-point requirements, singleton reduction) are proved in App. B. Crucially, Pareto-compliance statements hold conditional on a fixed reference point; in practice we update $\mathbf{r}(t)$ conservatively (monotone safeguard $r_k \leftarrow \max(r_k, \tilde{L}_k + \delta)$) to maintain positivity. We therefore treat $\phi(t)$ as a *priority signal* for planning within each epoch, not as a globally comparable progress metric across training.

Log-HV sensitivities as planning priorities. Differentiating (5) w.r.t. $\tilde{L}_k(t)$ (holding $\mathbf{r}(t)$ fixed) yields a closed-form marginal sensitivity,

$$w_k^{\text{HV}}(t) := \frac{1}{r_k(t) - \tilde{L}_k(t) + \varepsilon}, \quad (6)$$

which measures how strongly improving objective k would increase log-HV locally. The full derivation and the relationship between HV and log-HV gradients are provided in App. B.3.

Allocation plan. We convert sensitivities into an epoch-level allocation plan by tempering with the difficulty state $D_k(t)$ from Sec. 4.1. Define the difficulty-adjusted priority $a_k := w_k^{\text{HV}} / (1 + \gamma D_k)$; then

$$f_k(t) := a_k(t) / \sum_{j=1}^K a_j(t). \quad (7)$$

Intuitively, w_k^{HV} answers *which objective is most valuable for Pareto-compliant progress*, while difficulty tempering answers *how efficiently compute converts into progress*. Within epoch t , this induces a cumulative reference allocation $N_k^{\text{ref}}(m) := f_k(t) \cdot m$ at block m , which serves as the target tracked by the controller in Sec. 4.3. App. B.5 derives (7) from a proportional-fair planning objective.

4.3. Tactical Execution: PID Tracking of the Allocation Plan

The planner outputs an epoch-level target fraction $f(t) \in \Delta^K$, but execution is discrete: each block trains exactly one task. Tactical execution therefore solves a tracking problem: within epoch t , choose a task sequence $\{k_{t,m}\}_{m \geq 1}$ so that the realized counts match the reference trajectory $N_k^{\text{ref}}(m) := m f_k(t)$ from Sec. 4.2. We deliberately control *allocation counts* rather than losses: a scheduling decision changes counts deterministically by one, whereas losses are noisy and respond indirectly to a single block. This yields a well-conditioned feedback channel and a controller that is easy to audit via tracking plots.

Deficits and causal tracking error. Let $N_k(m) := \sum_{\tau=1}^m \mathbb{1}\{k_{t,\tau} = k\}$ be the number of blocks assigned to task k after executing m blocks in epoch t . At the *start* of block m (before choosing $k_{t,m}$), the system state is $N_k(m-1)$ and the desired cumulative allocation after executing this block is $N_k^{\text{ref}}(m) = m f_k(t)$. We therefore define the *pre-decision* deficit

$$e_k(m) := N_k^{\text{ref}}(m) - N_k(m-1). \quad (8)$$

Selecting task k at block m increments N_k by exactly 1 and leaves other N_j unchanged, inducing a direct, stable error dynamics (formalized in App. C).

PID logits and stochastic scheduling. We compute per-task control logits from the deficit, its running integral, and its discrete derivative:

$$\begin{aligned} I_k(m) &:= I_k(m-1) + e_k(m), \\ \Delta e_k(m) &:= e_k(m) - e_k(m-1), \end{aligned} \quad (9)$$

Algorithm 1 `ControlG`: sense \rightarrow plan \rightarrow control scheduling

Require: Graph G ; objectives $\{L_k\}_{k=1}^K$; epochs T ; block size B_{block} ; sensing period u

- 1: **[CTRL]** Initialize θ , per-task states D_k, \tilde{L}_k, r_k (App. A, B)
- 2: **for** epoch $t = 1, \dots, T$ **do**
- 3: **[CTRL]** Reset $N_k, N_k^{\text{ref}}, I_k, e_k^{\text{prev}} \leftarrow 0$ for all k
- 4: **for** block $m = 1, \dots, M$ **do**
- 5: **if** $m = 1$ or $(m-1) \bmod u = 0$ **then**
- 6: **[SENSE]** Compute $\text{RQ}_k, \text{Conf}_k$ on G ; update D_k, \tilde{L}_k (Sec. 4.1)
- 7: **[PLAN]** Update r_k ; compute w_k^{HV} , plan f (Sec. 4.2)
- 8: **end if**
- 9: **[CTRL]** $N_k^{\text{ref}} \leftarrow N_k^{\text{ref}} + f_k$; $e_k \leftarrow N_k^{\text{ref}} - N_k$; update $I_k, \Delta e_k, \nu_k$
- 10: **[CTRL]** $p \leftarrow (1 - \epsilon) \text{softmax}(\nu/\tau) + \frac{\epsilon}{K} \mathbf{1}$; sample $k_{t,m} \sim \text{Cat}(p)$
- 11: **[CTRL]** Run B_{block} steps on $L_{k_{t,m}}$; $N_{k_{t,m}} \leftarrow N_{k_{t,m}} + 1$; $e_k^{\text{prev}} \leftarrow e_k$
- 12: **end for**
- 13: **end for**

$$\nu_k(m) := K_P^{(k)} e_k(m) + K_I^{(k)} I_k(m) + K_D^{(k)} \Delta e_k(m). \quad (10)$$

The logits are mapped to a sampling distribution with explicit exploration,

$$p(m) := (1 - \epsilon) \text{softmax}\left(\frac{\nu(m)}{\tau}\right) + \frac{\epsilon}{K} \mathbf{1}, \quad k_{t,m} \sim \text{Cat}(p(m)). \quad (11)$$

Intuitively, the proportional term prioritizes tasks that are behind schedule, the integral term removes steady-state bias under fractional targets, and the derivative term damps oscillations. Exploration prevents starvation and provides a simple finite-horizon drought guarantee. Given the selected task $k_{t,m}$, we perform the single-task block update in Eq. (2), update the count $N_k(m)$, and repeat—completing the sense–plan–control loop at block time. Theoretical properties and implementation stabilizers are given in App. C.

5. Experiments

Our experiments are designed to test whether `ControlG` delivers consistent improvements over single-pretext and multi-pretext baselines while remaining computationally practical. Beyond accuracy, we also evaluate whether `ControlG` exhibits the behaviors our methodology is designed to guarantee: adaptation to nonstationarity (drift), resilience to objective conflicts (disagreement), and explicit prevention of objective starvation (drought). To keep the main paper concise, we present the primary downstream

tables in the main text and defer detailed hyperparameters, dataset statistics, ablations, and diagnostic plots to App. D.1.

5.1. Experimental setup

Datasets. We evaluate on nine benchmarks spanning homophilic, heterophilic, and large-scale regimes. The homophilic set includes citation networks (CORA, CITESEER, PUBMED) using Planetoid splits (Yang et al., 2016), collaboration networks (COAUTHOR-CS, COAUTHOR-PHYSICS) (Shchur et al., 2018), and WIKI-CS (Mernyei & Cangea, 2020). The heterophilic set includes CHAMELEON and SQUIRREL (Rozemberczki et al., 2019) and ACTOR (Pei et al., 2020). For scalability, we include OGBN-ARXIV from OGB (Hu et al., 2020). Dataset statistics and preprocessing details are summarized in App. D.2.

Pretext task pool (K=5). Following task pools used in prior multi-pretext work (Jin et al., 2021; Ju et al., 2022), we pretrain with a fixed pool of five complementary objectives: link prediction (p_{link}), masked feature reconstruction (p_{recon}), node–subgraph mutual-information contrast (p_{minsg}), representation decorrelation (p_{decor}), and METIS partition prediction (p_{par}). Intuitively, they cover local topology, feature denoising, augmentation-invariant local context, redundancy reduction, and mesoscale community structure. We provide precise loss definitions and task-specific hyperparameters in App. D.1.

Baselines. We compare against three categories. *Supervised*: GCN and GAT trained end-to-end on labels (Kipf, 2016; Veličković et al., 2017). *Single-pretext SSL*: representative graph SSL methods including DGI (Veličković et al., 2018), GRACE (You et al., 2020), MVGRL (Hassani & Khasahmadi, 2020), and BGRL (Thakoor et al., 2021). *Multi-pretext / multi-task*: weighting-based approaches such as AUTOSSL (Jin et al., 2021) and WAS (uniform or tuned weights), and Pareto/projection-style methods including PARETOGNN (Ju et al., 2022), PCGRAD (Yu et al., 2020), and CAGRAD (Liu et al., 2021).

Evaluation (3 downstream tasks). Following standard multi-task graph SSL practice (Ju et al., 2022), we freeze the pretrained encoder and evaluate transfer on: **node classification** (linear probe; accuracy), **link prediction** (logistic decoder; ROC-AUC and AP), and **node clustering** (K-means on embeddings; NMI). For link prediction, we ensure no edge leakage by removing validation/test edges from the training graph. Exact split protocols, probe hyperparameters, and evaluation settings are listed in App. D.3.

5.2. Main results

Random scheduling alone provides strong baselines. Before analyzing ControlG, we highlight a striking pattern: the *Random* scheduler—which simply samples a pretext

task uniformly at random for each block—often matches or outperforms sophisticated multi-task methods. On node clustering (Table 7), Random achieves an average rank of 5.0, beating AUTOSSL, WAS, PARETOGNN, PCGRAD, and CAGRAD. Similar patterns appear on link prediction (Table 6). This suggests that *temporal separation* of conflicting objectives—even without intelligent scheduling—reduces gradient interference compared to per-step gradient mixing.

Main comparison. Table 1 reports node classification accuracy across nine datasets. Link prediction (Table 6) and node clustering (Table 7) are deferred to App. D.5 and App. D.6; ControlG achieves the best average rank on all three tasks (1.4, 1.9, and 1.8, respectively). Several patterns emerge: (i) ControlG ranks first or second on 8 of 9 datasets for node classification, with particularly strong gains on homophilic graphs (Cora +1.5%, PubMed +1.1%, Co-CS +1.8% over the next-best method). (ii) On heterophilic graphs (Chameleon, Squirrel, Actor), where objective conflicts are more pronounced, ControlG remains competitive with the best single-pretext method (p_{recon}) while substantially outperforming weighting-based approaches like WAS. (iii) On the large-scale ogbn-arxiv, ControlG achieves 72.86%, a 1.2% improvement over CAGRAD, demonstrating scalability.

5.3. Ablations and diagnostics

Table 2 isolates the contribution of each ControlG component. We ablate: (i) state estimation signals by setting $\alpha=0$ (no spectral demand) or $\beta=0$ (no interference); (ii) the planner by replacing log-hypervolume allocation with a uniform target; and (iii) the controller by replacing deficit-based tracking with i.i.d. sampling from \mathbf{f} . A link-prediction ablation appears in App. D.7 (Table 8).

Key findings. Removing the planner (uniform \mathbf{f}) causes the largest drop (e.g., -3.4% on Cora, -3.4% on PubMed), confirming that adaptive allocation is essential. Disabling both state signals ($\alpha=\beta=0$) yields similar degradation, showing that the planner’s effectiveness depends on accurate difficulty estimates. Comparing the two signals: spectral demand (α) provides consistent gains across all graphs, while interference (β) matters most on heterophilic datasets (Chameleon, Squirrel), where cross-task conflicts are stronger. Finally, replacing the PID controller with i.i.d. sampling from \mathbf{f} degrades performance by 1–2%, validating that deficit tracking improves allocation fidelity.

Diagnostics. App. D.9 visualizes closed-loop behavior: task selection timelines (Fig. 4), deficit traces (Fig. 5), and state trajectories (Fig. 6). These confirm that the controller tracks the planned allocation and that state estimates adapt to training dynamics.

Method	Cora	CiteSeer	Chameleon	Squirrel	Actor	PubMed	Wiki-CS	Co-CS	Arxiv	Avg Rank
BGRL	77.14 \pm 2.2	35.28 \pm 2.1	64.87 \pm 1.3	46.11 \pm 1.2	31.22 \pm 0.5	79.94 \pm 1.2	80.36 \pm 0.3	93.05 \pm 0.4	71.24 \pm 0.8	9.2
DGI	75.64 \pm 1.6	63.84 \pm 1.6	66.27 \pm 0.9	48.17 \pm 1.0	30.46 \pm 0.7	81.28 \pm 1.1	77.95 \pm 0.9	93.17 \pm 0.4	70.86 \pm 0.6	9.6
GRACE	68.88 \pm 2.1	58.96 \pm 2.3	66.23 \pm 0.4	54.06 \pm 1.2	28.80 \pm 0.5	80.54 \pm 0.8	79.78 \pm 0.3	93.62 \pm 0.2	—	9.1
MVGRL	79.32 \pm 0.9	59.68 \pm 3.9	55.00 \pm 1.1	—	31.17 \pm 0.7	78.60 \pm 0.9	—	90.51 \pm 4.5	—	12.4
p_link	76.72 \pm 1.0	52.76 \pm 1.9	57.41 \pm 3.6	36.56 \pm 1.3	29.00 \pm 0.6	81.28 \pm 0.5	79.22 \pm 0.3	91.92 \pm 0.2	70.42 \pm 0.5	13.1
p_recon	78.76 \pm 0.5	64.86 \pm 1.5	69.39 \pm 1.3	52.33 \pm 0.8	27.75 \pm 0.4	76.28 \pm 0.9	79.88 \pm 0.4	94.85 \pm 0.3	71.08 \pm 0.4	6.8
p_minsg	76.44 \pm 1.1	61.74 \pm 0.8	64.78 \pm 1.6	47.61 \pm 0.9	29.16 \pm 0.7	80.76 \pm 1.0	79.95 \pm 0.2	93.44 \pm 0.3	70.94 \pm 0.6	10.2
p_decor	43.86 \pm 9.0	34.22 \pm 5.7	52.59 \pm 0.8	40.88 \pm 1.1	25.92 \pm 0.9	75.66 \pm 1.3	72.60 \pm 4.7	93.39 \pm 0.3	68.52 \pm 1.2	15.6
p_par	67.22 \pm 1.3	52.74 \pm 1.7	57.06 \pm 3.4	40.96 \pm 0.6	28.26 \pm 1.3	74.20 \pm 0.8	73.56 \pm 0.2	92.31 \pm 0.2	69.86 \pm 0.7	14.7
AutoSSL	80.30 \pm 1.5	64.72 \pm 1.0	70.09 \pm 2.0	49.99 \pm 3.0	29.76 \pm 0.7	80.80 \pm 0.7	79.82 \pm 0.3	93.61 \pm 0.2	—	6.4
WAS	74.12 \pm 3.3	57.66 \pm 3.5	57.59 \pm 6.3	43.52 \pm 2.2	29.68 \pm 0.5	78.62 \pm 2.1	77.40 \pm 1.6	92.62 \pm 1.3	70.68 \pm 0.9	12.9
Uniform	77.14 \pm 0.9	58.68 \pm 1.2	66.23 \pm 1.4	49.93 \pm 1.0	29.26 \pm 0.5	82.38 \pm 0.5	80.48 \pm 0.2	93.97 \pm 0.2	71.32 \pm 0.4	7.3
ParetoGNN	78.26 \pm 0.9	58.32 \pm 1.1	65.35 \pm 2.2	45.00 \pm 1.9	28.95 \pm 1.0	67.72 \pm 3.3	79.94 \pm 0.1	93.96 \pm 0.2	70.56 \pm 0.8	10.8
PCGrad	79.44 \pm 0.8	59.66 \pm 1.4	66.84 \pm 1.4	49.11 \pm 1.3	29.63 \pm 0.5	83.12 \pm 0.5	80.40 \pm 0.2	94.07 \pm 0.2	71.48 \pm 0.3	5.8
CAGrad	80.40 \pm 0.4	62.66 \pm 0.3	66.75 \pm 0.6	50.34 \pm 1.4	29.67 \pm 0.5	82.84 \pm 0.9	79.94 \pm 0.3	94.31 \pm 0.1	71.62 \pm 0.4	5.2
Random	79.06 \pm 0.3	58.10 \pm 1.3	63.07 \pm 1.8	46.22 \pm 0.7	29.57 \pm 1.0	80.56 \pm 0.8	80.10 \pm 0.2	93.39 \pm 0.2	71.18 \pm 0.5	9.4
Round-Robin	78.52 \pm 2.0	59.90 \pm 1.1	64.61 \pm 1.1	48.17 \pm 1.1	30.07 \pm 0.5	80.78 \pm 0.5	80.22 \pm 0.1	94.11 \pm 0.2	71.28 \pm 0.4	7.4
ControlG	81.92 \pm 0.9	66.48 \pm 1.1	69.54 \pm 1.0	53.18 \pm 0.9	31.20 \pm 0.6	84.24 \pm 0.7	80.45 \pm 0.3	96.14 \pm 0.2	72.86 \pm 0.3	1.4

Table 1. Node classification accuracy. Mean \pm 95% CI over 5 seeds. First, second, and third best methods per dataset are highlighted. Avg Rank is the mean rank across datasets (lower is better). ControlG achieves the best average rank, consistently performing among the top methods across both homophilic and heterophilic graphs.

Variant	Cora	CiteSeer	Chameleon	Squirrel	Actor	PubMed	Wiki-CS	Co-CS	Arxiv
ControlG (full)	81.92 \pm 0.9	66.48 \pm 1.1	69.54 \pm 1.0	53.18 \pm 0.9	31.20 \pm 0.6	84.24 \pm 0.7	80.45 \pm 0.3	96.14 \pm 0.2	72.86 \pm 0.3
w/o spectral demand ($\alpha=0$)	80.14 \pm 1.2	64.72 \pm 1.4	67.82 \pm 1.3	51.64 \pm 1.1	30.42 \pm 0.8	82.68 \pm 0.9	79.12 \pm 0.5	95.42 \pm 0.3	71.94 \pm 0.5
w/o interference ($\beta=0$)	80.86 \pm 1.0	65.34 \pm 1.2	68.26 \pm 1.1	52.12 \pm 1.0	30.68 \pm 0.7	83.42 \pm 0.8	79.68 \pm 0.4	95.78 \pm 0.2	72.28 \pm 0.4
w/o planner (uniform f)	78.52 \pm 1.4	62.86 \pm 1.6	65.48 \pm 1.5	49.86 \pm 1.3	29.56 \pm 0.9	80.86 \pm 1.1	77.54 \pm 0.6	94.56 \pm 0.4	70.42 \pm 0.7
w/o controller (i.i.d. from f)	80.28 \pm 1.1	64.96 \pm 1.3	67.94 \pm 1.2	51.82 \pm 1.0	30.54 \pm 0.7	82.96 \pm 0.8	79.24 \pm 0.4	95.52 \pm 0.3	71.76 \pm 0.5
w/o state signals ($\alpha=\beta=0$)	77.86 \pm 1.5	61.92 \pm 1.7	64.72 \pm 1.6	48.94 \pm 1.4	29.18 \pm 1.0	79.94 \pm 1.2	76.82 \pm 0.7	94.18 \pm 0.5	69.82 \pm 0.8

Table 2. Ablation study (node classification accuracy). Each row removes one component from ControlG. Removing the planner or both state signals ($\alpha=\beta=0$) causes the largest drops, confirming that adaptive allocation and state estimation are essential. The interference term (β) matters most on heterophilic graphs (Chameleon, Squirrel), while spectral demand (α) provides consistent gains.

5.4. Implementation details

We use a fixed GNN backbone (GCN/GAT variants) across all methods. For ControlG, each block executes B_{block} steps on a single pretext task; state estimation runs every u blocks on the full graph (or a memory-efficient probe for ogbn-arxiv). All hyperparameters are listed in App. D.4 (Tables 4–5). Per-step timings (Table 9) show that ControlG incurs modest overhead but remains 5–15 \times faster than AUTOSL and PAREOGNN.

6. Conclusion

We introduced ControlG, a control-theoretic framework that, to the best of our knowledge, is the first to cast multi-objective graph self-supervised learning as a closed-loop scheduling problem with explicit allocation tracking. Rather than forcing every parameter update to blend signals from competing objectives—a design that leads to *Disagreement*

(conflict-induced negative transfer), *Drift* (nonstationary objective utility), and *Drought* (hidden starvation of under-served objectives)—ControlG coordinates pretext tasks through feedback-controlled temporal allocation: estimating per-objective difficulty via spectral demand and interference signals, planning target budgets via a Pareto-aware log-hypervolume planner, and executing discrete single-task blocks with a deficit-tracking PID controller. Across nine datasets spanning homophilic, heterophilic, and large-scale regimes, ControlG achieves the best average rank on node classification, link prediction, and node clustering, with particularly strong gains where gradient conflicts are most pronounced. The training process is fully auditable, revealing which objectives drove learning and when—providing both performance improvements and interpretability that we hope will serve as a useful template for principled multi-task learning.

Impact Statement

This work advances self-supervised representation learning on graphs by introducing a principled framework for coordinating multiple pretext objectives. Improved graph representations have broad applicability across scientific, industrial, and societal domains: molecular and protein embeddings can accelerate drug discovery; social network embeddings can improve community detection and misinformation identification; and the label-efficiency of self-supervised methods is valuable where annotation is expensive. The interpretability of ControlG’s scheduling mechanism—auditing which objectives drove learning—represents a step toward more transparent machine learning systems.

However, improved embeddings could be misused for invasive profiling, and GNNs may inherit biases from underlying graph structures. We encourage fairness audits before deployment in sensitive applications. All experiments used publicly available benchmarks, and we do not foresee dual-use concerns beyond those inherent to graph representation learning broadly.

References

Chen, Z., Badrinarayanan, V., Lee, C.-Y., and Rabinovich, A. Gradnorm: Gradient normalization for adaptive loss balancing in deep multitask networks. In *International conference on machine learning*, pp. 794–803. PMLR, 2018.

Fan, T., Wu, L., Huang, Y., Lin, H., Tan, C., Gao, Z., and Li, S. Z. Decoupling weighing and selecting for integrating multiple graph pre-training tasks. *arXiv preprint arXiv:2403.01400*, 2024.

Fang, T., Zhou, W., Sun, Y., Han, K., Ma, L., and Yang, Y. Exploring correlations of self-supervised tasks for graphs. In *International Conference on Machine Learning*, 2024.

Guerreiro, A. P., Fonseca, C. M., and Paquete, L. The hypervolume indicator: Problems and algorithms. *arXiv preprint arXiv:2005.00515*, 2020.

Guo, M., Haque, A., Huang, D.-A., Yeung, S., and Fei-Fei, L. Dynamic task prioritization for multitask learning. In *European Conference on Computer Vision*, 2018a. URL <https://api.semanticscholar.org/CorpusID:52952193>.

Guo, M., Haque, A., Huang, D.-A., Yeung, S., and Fei-Fei, L. Dynamic task prioritization for multitask learning. In *Proceedings of the European conference on computer vision (ECCV)*, pp. 270–287, 2018b.

Hassani, K. and Khasahmadi, A. H. Contrastive multi-view representation learning on graphs. In *International conference on machine learning*, pp. 4116–4126. PMLR, 2020.

Hou, Z., Liu, X., Cen, Y., Dong, Y., Yang, H., Wang, C., and Tang, J. Graphmae: Self-supervised masked graph autoencoders. In *Proceedings of the 28th ACM SIGKDD conference on knowledge discovery and data mining*, pp. 594–604, 2022.

Hu, W., Fey, M., Zitnik, M., Dong, Y., Ren, H., Liu, B., Catasta, M., and Leskovec, J. Open graph benchmark: Datasets for machine learning on graphs. *ArXiv*, abs/2005.00687, 2020. URL <https://api.semanticscholar.org/CorpusID:218487328>.

Jin, W., Liu, X., Zhao, X., Ma, Y., Shah, N., and Tang, J. Automated self-supervised learning for graphs. *arXiv preprint arXiv:2106.05470*, 2021.

Ju, M., Zhao, T., Wen, Q., Yu, W., Shah, N., Ye, Y., and Zhang, C. Multi-task self-supervised graph neural networks enable stronger task generalization. *arXiv preprint arXiv:2210.02016*, 2022.

Ju, W., Wang, Y., Qin, Y., Mao, Z., Xiao, Z., Luo, J., Yang, J., Gu, Y., Wang, D., Long, Q., et al. Towards graph contrastive learning: A survey and beyond. *arXiv preprint arXiv:2405.11868*, 2024.

Kendall, A., Gal, Y., and Cipolla, R. Multi-task learning using uncertainty to weigh losses for scene geometry and semantics. In *Proceedings of the IEEE conference on computer vision and pattern recognition*, pp. 7482–7491, 2018.

Kipf, T. Semi-supervised classification with graph convolutional networks. *arXiv preprint arXiv:1609.02907*, 2016.

Laforgue, P., Vecchia, A. D., Cesa-Bianchi, N., and Rosasco, L. Adatask: Adaptive multitask online learning. *ArXiv*, abs/2205.15802, 2022. URL <https://api.semanticscholar.org/CorpusID:249209943>.

Liu, B., Liu, X., Jin, X., Stone, P., and Liu, Q. Conflict-averse gradient descent for multi-task learning. *Advances in Neural Information Processing Systems*, 34:18878–18890, 2021.

Liu, Y., Jin, M., Pan, S., Zhou, C., Zheng, Y., Xia, F., and Yu, P. S. Graph self-supervised learning: A survey. *IEEE transactions on knowledge and data engineering*, 35(6):5879–5900, 2022.

Mernyei, P. and Cangea, C. Wiki-cs: A wikipedia-based benchmark for graph neural networks.

ArXiv, abs/2007.02901, 2020. URL <https://api.semanticscholar.org/CorpusID:220364329>.

Navon, A., Shamsian, A., Achituv, I., Maron, H., Kawaguchi, K., Chechik, G., and Fetaya, E. Multi-task learning as a bargaining game. *arXiv preprint arXiv:2202.01017*, 2022.

Nt, H. and Maehara, T. Revisiting graph neural networks: All we have is low-pass filters. *arXiv preprint arXiv:1905.09550*, 2019.

Pei, H., Wei, B., Chang, K. C.-C., Lei, Y., and Yang, B. Geom-gcn: Geometric graph convolutional networks. ArXiv, abs/2002.05287, 2020. URL <https://api.semanticscholar.org/CorpusID:210843644>.

Rozemberczki, B., Allen, C., and Sarkar, R. Multi-scale attributed node embedding. ArXiv, abs/1909.13021, 2019. URL <https://api.semanticscholar.org/CorpusID:203593476>.

Sener, O. and Koltun, V. Multi-task learning as multi-objective optimization. *Advances in neural information processing systems*, 31, 2018.

Shchur, O., Mumme, M., Bojchevski, A., and Günnemann, S. Pitfalls of graph neural network evaluation. ArXiv, abs/1811.05868, 2018. URL <https://api.semanticscholar.org/CorpusID:53303554>.

Shreedhar, M. and Varghese, G. Efficient fair queuing using deficit round-robin. *IEEE/ACM Transactions on networking*, 4(3):375–385, 1996.

Thakoor, S., Tallec, C., Azar, M. G., Azabou, M., Dyer, E. L., Munos, R., Veličković, P., and Valko, M. Large-scale representation learning on graphs via bootstrapping. *arXiv preprint arXiv:2102.06514*, 2021.

Veličković, P., Cucurull, G., Casanova, A., Romero, A., Lio, P., and Bengio, Y. Graph attention networks. *arXiv preprint arXiv:1710.10903*, 2017.

Veličković, P., Fedus, W., Hamilton, W. L., Liò, P., Bengio, Y., and Hjelm, R. D. Deep graph infomax. *arXiv preprint arXiv:1809.10341*, 2018.

Von Luxburg, U. A tutorial on spectral clustering. *Statistics and computing*, 17(4):395–416, 2007.

Yang, Z., Cohen, W. W., and Salakhutdinov, R. Revisiting semi-supervised learning with graph embeddings. In *International Conference on Machine Learning*, 2016. URL <https://api.semanticscholar.org/CorpusID:7008752>.

You, Y., Chen, T., Sui, Y., Chen, T., Wang, Z., and Shen, Y. Graph contrastive learning with augmentations. *Advances in neural information processing systems*, 33:5812–5823, 2020.

Yu, T., Kumar, S., Gupta, A., Levine, S., Hausman, K., and Finn, C. Gradient surgery for multi-task learning. *Advances in neural information processing systems*, 33: 5824–5836, 2020.

Zhu, Y., Xu, Y., Yu, F., Liu, Q., Wu, S., and Wang, L. Deep graph contrastive representation learning. *arXiv preprint arXiv:2006.04131*, 2020.

Zhu, Y., Xu, Y., Yu, F., Liu, Q., Wu, S., and Wang, L. Graph contrastive learning with adaptive augmentation. In *Proceedings of the web conference 2021*, pp. 2069–2080, 2021.

Appendix: Table of Contents

Appendix Contents:

A State Estimation: Theory and Proofs

- A.1 Normalized Laplacian preliminaries
- A.2 Dirichlet energy identities
- A.3 Spectral meaning of the Rayleigh quotient
- A.4 High RQ implies reduced progress under low-pass attenuation
- A.5 Interference and MGDA relevance
- A.6 Why MGDA weights identify locally relevant objectives
- A.7 Composite difficulty aggregation

B Log-Hypervolume Planning: Definitions and Proofs

- B.1 Preliminaries: dominance and hypervolume
- B.2 Pareto compliance for fixed reference point
- B.3 Log-hypervolume sensitivities
- B.4 Reference point specification and positivity
- B.5 Deriving the allocation plan

C Tactical Execution: Deficit Dynamics and Guarantees

- C.1 Deficit dynamics and basic identities
- C.2 Worst-case tracking guarantee in the max-deficit limit
- C.3 Relation to the PID-softmax controller
- C.4 Starvation prevention under explicit exploration
- C.5 Implementation stabilizers

D Additional Experimental Details

- D.1 Pretext task objectives
- D.2 Dataset statistics and preprocessing
- D.3 Evaluation protocols
- D.4 Hyperparameters and reproducibility
- D.5 Additional results: link prediction
- D.6 Additional results: node clustering
- D.7 Ablations
- D.8 Compute and overhead
- D.9 Diagnostics: scheduling, tracking, and state

See next page for notation summary.

Notation Summary

Key notation used throughout the paper, organized by category.

Symbol	Description	Symbol	Description
<i>Graph, Encoder, and Spectral Quantities</i>			
$G = (V, E, \mathbf{X})$	Attributed graph	\mathbf{A}, \mathbf{D}	Adjacency, degree matrices
$n = V $	Number of nodes	$\mathbf{X} \in \mathbb{R}^{n \times d}$	Node features
$f_\theta, \mathbf{Z} \in \mathbb{R}^{n \times h}$	Encoder, embeddings	z_v	Embedding of node v
$\tilde{\mathbf{L}}$	Normalized Laplacian	$\mathcal{E}(\mathbf{H})$	Dirichlet energy
RQ_k	Rayleigh quotient (spectral demand)	$H_k \in \mathbb{R}^{n \times h}$	Representation-gradient field
<i>Objectives, Losses, and Gradients</i>			
K	Number of objectives	\mathcal{T}_k	Pretext task k
$L_k(\theta)$	Loss (deterministic)	$\mathcal{L}_k(\theta)$	Expected loss (stochastic)
$\tilde{L}_k, \tilde{\ell}$	Normalized loss, vector	$g_k = \nabla_\theta L_k$	Parameter gradient
\hat{g}_k	Unit-normalized gradient	Δ^K	Probability simplex
$\lambda^*, g_{\text{mix}}$	MGDA weights, mixed gradient	Conf_k	Interference score
<i>State Estimation and Planning</i>			
D_k	Difficulty state	$\alpha, \beta, \gamma, \rho$	Difficulty hyperparams
$\mathbf{r}(t)$	HV reference point	$\text{HV}(t), \phi(t)$	Hypervolume, log-HV
w_k^{HV}	Log-HV sensitivity	a_k	Adjusted priority
$f(t) \in \Delta^K$	Allocation plan	δ, ε	Margin, stabilizer
<i>Timescales and Control</i>			
t, T	Epoch index, total epochs	m, M	Block index, blocks/epoch
u	Sensing period	$B_{\text{ep}}, B_{\text{block}}$	Batches/epoch, batches/block
$N_k(m)$	Cumulative task- k count	$N_k^{\text{ref}}(m)$	Reference count
$e_k(m)$	Pre-decision deficit	$I_k(m), \Delta e_k$	Integral, derivative
$\nu_k(m)$	PID control logit	K_P, K_I, K_D	PID gains
τ, ϵ	Temperature, exploration	$k_{t,m}$	Selected task
<i>Miscellaneous</i>			
η	Learning rate	$\mathbb{1}\{\cdot\}$	Indicator function
$\text{clip}(x, [a, b])$	Clipping function	$[x]_+$	Positive part

Note: We use $\tilde{\ell}$ for the normalized loss vector to distinguish from the normalized Laplacian $\tilde{\mathbf{L}}$.

A. State Estimation: Theory and Proofs

This appendix provides formal derivations and proofs for the state-estimation quantities used in Sec. 4.1. Throughout, we assume an undirected graph unless stated otherwise so that the normalized Laplacian is symmetric PSD and admits an orthonormal eigenbasis.

A.1. Normalized Laplacian preliminaries

Let $G = (V, E)$ be an undirected weighted graph with symmetric adjacency $\mathbf{A} \in \mathbb{R}^{n \times n}$ ($n = |V|$), degrees $d_i = \sum_j A_{ij}$, and $\mathbf{D} = \text{diag}(d_1, \dots, d_n)$. The symmetric normalized Laplacian is

$$\tilde{\mathbf{L}} := \mathbf{I} - \mathbf{D}^{-1/2} \mathbf{A} \mathbf{D}^{-1/2}.$$

Claim A.1 (Eigenvalue range of the normalized Laplacian). *All eigenvalues of $\tilde{\mathbf{L}}$ lie in $[0, 2]$.*

Proof. Let $\tilde{\mathbf{S}} := \mathbf{D}^{-1/2} \mathbf{A} \mathbf{D}^{-1/2}$, so $\tilde{\mathbf{L}} = \mathbf{I} - \tilde{\mathbf{S}}$. Since $\tilde{\mathbf{S}}$ is symmetric, its spectral radius equals $\|\tilde{\mathbf{S}}\|_2 = \max_{\|x\|_2=1} |x^\top \tilde{\mathbf{S}} x|$. For any $x \in \mathbb{R}^n$, define $y := \mathbf{D}^{-1/2} x$. Then

$$x^\top \tilde{\mathbf{S}} x = x^\top \mathbf{D}^{-1/2} \mathbf{A} \mathbf{D}^{-1/2} x = y^\top \mathbf{A} y = \sum_{i,j} A_{ij} y_i y_j.$$

Assuming no self-loops (or absorbing them into the diagonal similarly), apply the inequality $2|ab| \leq a^2 + b^2$ edgewise to bound the absolute value:

$$|A_{ij} y_i y_j| \leq \frac{A_{ij}}{2} (y_i^2 + y_j^2).$$

Summing over all pairs yields

$$|y^\top \mathbf{A} y| \leq \sum_{i,j} |A_{ij} y_i y_j| \leq \frac{1}{2} \sum_{i,j} A_{ij} (y_i^2 + y_j^2) = \sum_i \left(\sum_j A_{ij} \right) y_i^2 = \sum_i d_i y_i^2 = x^\top x.$$

Thus $|x^\top \tilde{\mathbf{S}} x| \leq x^\top x$ for all x , which directly implies $\|\tilde{\mathbf{S}}\|_2 \leq 1$. Equivalently, all eigenvalues of $\tilde{\mathbf{S}}$ lie in $[-1, 1]$. Therefore eigenvalues of $\tilde{\mathbf{L}} = \mathbf{I} - \tilde{\mathbf{S}}$ lie in $[0, 2]$. (This is also a standard spectral graph theory fact.) \square

A.2. Dirichlet energy identities

Claim A.2 (Edge-domain form of the normalized Laplacian quadratic form). *For any vector $x \in \mathbb{R}^n$,*

$$x^\top \tilde{\mathbf{L}} x = \frac{1}{2} \sum_{i,j=1}^n A_{ij} \left(\frac{x_i}{\sqrt{d_i}} - \frac{x_j}{\sqrt{d_j}} \right)^2.$$

Proof. Let $y := \mathbf{D}^{-1/2} x$. Then

$$x^\top \tilde{\mathbf{L}} x = x^\top x - x^\top \mathbf{D}^{-1/2} \mathbf{A} \mathbf{D}^{-1/2} x = y^\top \mathbf{D} y - y^\top \mathbf{A} y.$$

Expand each term:

$$y^\top \mathbf{D} y = \sum_{i=1}^n d_i y_i^2, \quad y^\top \mathbf{A} y = \sum_{i,j=1}^n A_{ij} y_i y_j.$$

Use $d_i = \sum_j A_{ij}$ to rewrite $\sum_i d_i y_i^2 = \sum_{i,j} A_{ij} y_i^2$. By symmetry of A , also $\sum_{i,j} A_{ij} y_i^2 = \sum_{i,j} A_{ij} y_j^2$. Hence

$$\sum_i d_i y_i^2 = \frac{1}{2} \sum_{i,j} A_{ij} y_i^2 + \frac{1}{2} \sum_{i,j} A_{ij} y_j^2.$$

Therefore

$$\begin{aligned} x^\top \tilde{\mathbf{L}} x &= \frac{1}{2} \sum_{i,j} A_{ij} y_i^2 + \frac{1}{2} \sum_{i,j} A_{ij} y_j^2 - \sum_{i,j} A_{ij} y_i y_j \\ &= \frac{1}{2} \sum_{i,j} A_{ij} (y_i^2 + y_j^2 - 2y_i y_j) = \frac{1}{2} \sum_{i,j} A_{ij} (y_i - y_j)^2. \end{aligned}$$

Substituting $y_i = x_i / \sqrt{d_i}$ yields the claim. \square

Claim A.3 (Matrix-signal extension). *For any matrix signal $H \in \mathbb{R}^{n \times h}$ with rows $H_{i,:}$,*

$$\text{tr}(H^\top \tilde{\mathbf{L}} H) = \frac{1}{2} \sum_{i,j=1}^n A_{ij} \left\| \frac{H_{i,:}}{\sqrt{d_i}} - \frac{H_{j,:}}{\sqrt{d_j}} \right\|_2^2.$$

Proof. Write $H = [x^{(1)}, \dots, x^{(h)}]$ by columns. Then

$$\text{tr}(H^\top \tilde{\mathbf{L}} H) = \sum_{\ell=1}^h (x^{(\ell)})^\top \tilde{\mathbf{L}} x^{(\ell)}.$$

Apply Claim A.2 to each column $x^{(\ell)}$ and sum over ℓ :

$$\sum_{\ell=1}^h \frac{1}{2} \sum_{i,j} A_{ij} \left(\frac{x_i^{(\ell)}}{\sqrt{d_i}} - \frac{x_j^{(\ell)}}{\sqrt{d_j}} \right)^2 = \frac{1}{2} \sum_{i,j} A_{ij} \sum_{\ell=1}^h \left(\frac{x_i^{(\ell)}}{\sqrt{d_i}} - \frac{x_j^{(\ell)}}{\sqrt{d_j}} \right)^2,$$

and the inner sum is exactly the squared Euclidean norm of the row difference, proving the result. \square

A.3. Spectral meaning of the Rayleigh quotient

Claim A.4 (Eigenbasis decomposition for matrix Dirichlet energy). *Let $\tilde{\mathbf{L}} = \mathbf{U} \Lambda \mathbf{U}^\top$ with orthonormal \mathbf{U} and $\Lambda = \text{diag}(\lambda_1, \dots, \lambda_n)$. Then for any $H \in \mathbb{R}^{n \times h}$,*

$$\text{tr}(H^\top \tilde{\mathbf{L}} H) = \sum_{i=1}^n \lambda_i \|\mathbf{U}_i^\top H\|_2^2, \quad \|H\|_F^2 = \sum_{i=1}^n \|\mathbf{U}_i^\top H\|_2^2.$$

Consequently, for $H \neq 0$ and ignoring the stabilizer,

$$\frac{\text{tr}(H^\top \tilde{\mathbf{L}} H)}{\|H\|_F^2} = \frac{\sum_{i=1}^n \lambda_i w_i}{\sum_{i=1}^n w_i}, \quad w_i := \|\mathbf{U}_i^\top H\|_2^2 \geq 0,$$

i.e., the Rayleigh quotient is a convex combination (weighted average) of eigenvalues.

Proof. Using cyclicity of trace and $\mathbf{U}^\top \mathbf{U} = \mathbf{I}$,

$$\text{tr}(H^\top \tilde{\mathbf{L}} H) = \text{tr}(H^\top \mathbf{U} \Lambda \mathbf{U}^\top H) = \text{tr}((\mathbf{U}^\top H)^\top \Lambda (\mathbf{U}^\top H)).$$

Let $\hat{H} := \mathbf{U}^\top H$ and denote its i -th row by $\hat{H}_{i,:} = \mathbf{U}_i^\top H$. Since Λ is diagonal,

$$\text{tr}(\hat{H}^\top \Lambda \hat{H}) = \sum_{i=1}^n \lambda_i \|\hat{H}_{i,:}\|_2^2 = \sum_{i=1}^n \lambda_i \|\mathbf{U}_i^\top H\|_2^2.$$

Similarly, $\|H\|_F^2 = \|\mathbf{U}^\top H\|_F^2 = \sum_i \|\mathbf{U}_i^\top H\|_2^2$ by orthonormality of \mathbf{U} . The Rayleigh-quotient expression follows. \square

A.4. Why high Rayleigh quotient implies reduced attainable progress under low-pass attenuation

This section makes explicit the modeling assumption used in Sec. 4.1.1 and derives a rigorous upper bound connecting spectral demand to first-order progress.

Assumption A.5 (Low-pass attenuation model for representation updates). Fix an objective k and its representation-gradient field $H_k = \nabla_Z L_k(\theta; G) \in \mathbb{R}^{n \times h}$ at the current parameters θ . Assume that, in a local linearization, a single update on objective k induces an effective representation change of the form

$$\Delta Z \approx -\eta p(\tilde{\mathbf{L}}) H_k,$$

where $p(\tilde{\mathbf{L}}) = \mathbf{U} \text{diag}(p(\lambda_1), \dots, p(\lambda_n)) \mathbf{U}^\top$ is a symmetric graph spectral filter with a non-increasing frequency response $p(\lambda)$ (low-pass attenuation).

Lemma A.6 (First-order progress under Assumption A.5). *Under Assumption A.5, the first-order change in objective k satisfies*

$$L_k(\theta + \Delta\theta) \approx L_k(\theta) - \eta \text{tr}(H_k^\top p(\tilde{\mathbf{L}}) H_k),$$

and therefore the first-order decrease magnitude is

$$\Delta_k := \eta \text{tr}(H_k^\top p(\tilde{\mathbf{L}}) H_k) = \eta \sum_{i=1}^n p(\lambda_i) \|\mathbf{U}_i^\top H_k\|_2^2.$$

Proof. By first-order Taylor expansion in representation space, $L_k(Z + \Delta Z) \approx L_k(Z) + \langle \nabla_Z L_k(Z), \Delta Z \rangle_F = L_k(Z) + \langle H_k, \Delta Z \rangle_F$. Substituting $\Delta Z \approx -\eta p(\tilde{\mathbf{L}}) H_k$ gives

$$L_k(Z + \Delta Z) \approx L_k(Z) - \eta \langle H_k, p(\tilde{\mathbf{L}}) H_k \rangle_F = L_k(Z) - \eta \text{tr}(H_k^\top p(\tilde{\mathbf{L}}) H_k).$$

Using the eigendecomposition of $p(\tilde{\mathbf{L}})$ and the same trace manipulation as in Claim A.4 yields the spectral sum form. \square

Lemma A.7 (High Rayleigh quotient forces mass at high frequencies). *Let $w_i := \|\mathbf{U}_i^\top H_k\|_2^2$ and $W := \sum_i w_i = \|H_k\|_F^2$. Define normalized weights $\mu_i := w_i/W$ (so $\sum_i \mu_i = 1$), and define the Rayleigh quotient without stabilizer $r := \sum_i \lambda_i \mu_i$. For any cutoff $\lambda_c \in [0, \lambda_{\max}]$ with $\lambda_{\max} := \lambda_n$, let*

$$\pi_{\geq \lambda_c} := \sum_{i: \lambda_i \geq \lambda_c} \mu_i \quad (\text{fraction of gradient energy at frequencies } \geq \lambda_c).$$

Then

$$\pi_{\geq \lambda_c} \geq \max \left\{ 0, \frac{r - \lambda_c}{\lambda_{\max} - \lambda_c} \right\}.$$

Proof. Write $r = \sum_{\lambda_i < \lambda_c} \lambda_i \mu_i + \sum_{\lambda_i \geq \lambda_c} \lambda_i \mu_i$. Since $\lambda_i \leq \lambda_c$ on the first sum and $\lambda_i \leq \lambda_{\max}$ on the second sum,

$$r \leq \lambda_c \sum_{\lambda_i < \lambda_c} \mu_i + \lambda_{\max} \sum_{\lambda_i \geq \lambda_c} \mu_i = \lambda_c (1 - \pi_{\geq \lambda_c}) + \lambda_{\max} \pi_{\geq \lambda_c}.$$

Rearranging yields $\pi_{\geq \lambda_c} \geq (r - \lambda_c) / (\lambda_{\max} - \lambda_c)$. If $r \leq \lambda_c$ the bound is nonpositive, so the trivial bound 0 applies; combining gives the stated max form. \square

Proposition A.8 (Upper bound on attainable first-order progress decreases with spectral demand). *Under Assumption A.5 and Lemma A.6, fix any cutoff $\lambda_c \in [0, \lambda_{\max}]$. Let $p(\lambda)$ be non-increasing. Define $p_0 := p(0)$ and $p_c := p(\lambda_c)$. Then for the per-energy progress ratio*

$$\bar{\Delta}_k := \frac{\Delta_k}{\eta \|H_k\|_F^2} = \sum_{i=1}^n p(\lambda_i) \mu_i,$$

we have the bound

$$\bar{\Delta}_k \leq p_0 - (p_0 - p_c) \pi_{\geq \lambda_c},$$

and hence, in terms of the Rayleigh quotient $r = \sum_i \lambda_i \mu_i$,

$$\bar{\Delta}_k \leq p_0 - (p_0 - p_c) \max \left\{ 0, \frac{r - \lambda_c}{\lambda_{\max} - \lambda_c} \right\}.$$

In particular, for any fixed λ_c and λ_{\max} , this upper bound is a non-increasing function of r ; thus larger Rayleigh quotient implies a smaller upper bound on first-order progress per unit gradient energy under low-pass attenuation.

Proof. Split the sum into low and high frequency parts:

$$\bar{\Delta}_k = \sum_{\lambda_i < \lambda_c} p(\lambda_i) \mu_i + \sum_{\lambda_i \geq \lambda_c} p(\lambda_i) \mu_i.$$

Since $p(\lambda)$ is non-increasing, for $\lambda_i < \lambda_c$ we have $p(\lambda_i) \leq p(0) = p_0$, and for $\lambda_i \geq \lambda_c$ we have $p(\lambda_i) \leq p(\lambda_c) = p_c$. Therefore,

$$\bar{\Delta}_k \leq p_0 \sum_{\lambda_i < \lambda_c} \mu_i + p_c \sum_{\lambda_i \geq \lambda_c} \mu_i = p_0(1 - \pi_{\geq \lambda_c}) + p_c \pi_{\geq \lambda_c} = p_0 - (p_0 - p_c) \pi_{\geq \lambda_c}.$$

Substituting the lower bound on $\pi_{\geq \lambda_c}$ from Lemma A.7 yields the inequality in terms of r . Since $(p_0 - p_c) \geq 0$ and the max term is non-decreasing in r , the bound is non-increasing in r . \square

Remark A.9 (How this supports “difficulty” in Sec. 4.1.1). For fixed $\|H_k\|_F$ and η , Proposition A.8 gives a decreasing upper bound on the attainable first-order decrease as the Rayleigh quotient increases. Thus achieving a target decrease in L_k requires at least $\Omega(1/\bar{\Delta}_k)$ steps, which grows as the spectral demand (Rayleigh quotient) increases. This is the formal sense in which RQ_k can be used as a difficulty proxy under Assumption A.5.

A.5. Interference and MGDA relevance

Claim A.10 (Negative alignment implies first-order interference). *Let $g_k(\theta) = \nabla_{\theta} L_k(\theta; G)$. For $\theta^+ = \theta - \eta g_k(\theta)$ with $\eta > 0$,*

$$L_j(\theta^+) = L_j(\theta) - \eta \langle g_j(\theta), g_k(\theta) \rangle + o(\eta).$$

In particular, if $\langle g_j, g_k \rangle < 0$, a descent step on k increases L_j to first order.

Proof. This is the first-order Taylor expansion: $L_j(\theta - \eta g_k) = L_j(\theta) + \langle \nabla_{\theta} L_j(\theta), -\eta g_k(\theta) \rangle + o(\eta)$, and $\nabla_{\theta} L_j(\theta) = g_j(\theta)$. \square

Theorem A.11 (Pareto stationarity and convex hull of gradients). *Fix gradients $g_1, \dots, g_K \in \mathbb{R}^d$ at a point θ . Define first-order Pareto stationarity (PS) as: there does not exist a direction $d \in \mathbb{R}^d$ such that $\langle g_k, d \rangle < 0$ for all k . Let $\mathcal{C} := \text{conv}\{g_1, \dots, g_K\}$. Then θ is PS if and only if $\mathbf{0} \in \mathcal{C}$.*

Proof. (\Rightarrow) Suppose $\mathbf{0} \notin \mathcal{C}$. Since \mathcal{C} is compact and convex and $\mathbf{0}$ is a point outside it, the strong separating hyperplane theorem implies there exists $d \neq 0$ and $c > 0$ such that $\langle d, g \rangle \geq c$ for all $g \in \mathcal{C}$. In particular, for each extreme point $g_k \in \mathcal{C}$ we have $\langle d, g_k \rangle \geq c > 0$, hence $\langle -d, g_k \rangle \leq -c < 0$ for all k . Thus $-d$ is a common descent direction, contradicting PS.

(\Leftarrow) Conversely, if there exists d such that $\langle g_k, d \rangle < 0$ for all k , then for any convex combination $g = \sum_k \lambda_k g_k$ with $\lambda \in \Delta^K$ we have $\langle g, d \rangle = \sum_k \lambda_k \langle g_k, d \rangle < 0$. In particular $\langle \mathbf{0}, d \rangle = 0$ cannot satisfy this strict inequality, so $\mathbf{0}$ cannot belong to the convex hull \mathcal{C} . Therefore, if $\mathbf{0} \in \mathcal{C}$, no such common descent direction exists; hence θ is PS. \square

Theorem A.12 (MGDA as projection; descent unless Pareto-stationary). *Let $G = [g_1, \dots, g_K] \in \mathbb{R}^{d \times K}$ and consider the convex program*

$$\min_{\lambda \in \Delta^K} \frac{1}{2} \|G\lambda\|_2^2.$$

Let λ^ be an optimizer and define $g_{\text{mix}} := G\lambda^* \in \mathcal{C}$. Then: (i) g_{mix} is the Euclidean projection of $\mathbf{0}$ onto the convex hull \mathcal{C} ; (ii) if $g_{\text{mix}} = \mathbf{0} \in \mathcal{C}$ and θ is Pareto-stationary (Theorem A.11); (iii) if $g_{\text{mix}} \neq \mathbf{0}$ then $d := -g_{\text{mix}}$ is a common descent direction and moreover*

$$\langle g_k, d \rangle \leq -\|g_{\text{mix}}\|_2^2 \quad \text{for all } k.$$

Proof. (i) The set $\mathcal{C} = \{G\lambda : \lambda \in \Delta^K\}$ is exactly the feasible set of convex combinations. Minimizing $\|G\lambda\|_2^2/2$ is equivalent to minimizing $\|g\|_2^2/2$ over $g \in \mathcal{C}$, hence g_{mix} is the closest point in \mathcal{C} to the origin, i.e., the projection.

(ii) If $g_{\text{mix}} = \mathbf{0}$, then $\mathbf{0} \in \mathcal{C}$ by definition of \mathcal{C} , and PS follows from Theorem A.11.

(iii) Projection onto a closed convex set satisfies the variational inequality: for all $g \in \mathcal{C}$, $\langle g - g_{\text{mix}}, \mathbf{0} - g_{\text{mix}} \rangle \leq 0$. Substituting $\mathbf{0} - g_{\text{mix}} = -g_{\text{mix}}$ gives

$$\langle g - g_{\text{mix}}, g_{\text{mix}} \rangle \geq 0 \quad \text{for all } g \in \mathcal{C}.$$

In particular, for each extreme point $g = g_k$, we obtain $\langle g_k, g_{\text{mix}} \rangle \geq \langle g_{\text{mix}}, g_{\text{mix}} \rangle = \|g_{\text{mix}}\|_2^2$. Therefore $\langle g_k, -g_{\text{mix}} \rangle \leq -\|g_{\text{mix}}\|_2^2$ for all k , proving $-g_{\text{mix}}$ is a common descent direction with the stated margin. \square

A.6. Why MGDA weights identify locally relevant objectives

Proposition A.13 (KKT characterization of MGDA weights). *Let λ^* solve $\min_{\lambda \in \Delta^K} \frac{1}{2} \|G\lambda\|_2^2$ and $g_{\text{mix}} = G\lambda^*$. Then there exists a scalar ν such that for every k ,*

$$\langle g_k, g_{\text{mix}} \rangle \geq \|g_{\text{mix}}\|_2^2,$$

with equality for all k in the active set $\mathcal{A} := \{k : \lambda_k^ > 0\}$. Equivalently, active gradients are exactly those lying on the supporting face of \mathcal{C} orthogonal to g_{mix} .*

Proof. Consider the Lagrangian

$$\mathcal{L}(\lambda, \mu, \nu) = \frac{1}{2} \|G\lambda\|_2^2 - \mu^\top \lambda + \nu(\mathbf{1}^\top \lambda - 1),$$

with multipliers $\mu \succeq 0$ for $\lambda \succeq 0$ and $\nu \in \mathbb{R}$ for $\mathbf{1}^\top \lambda = 1$. Stationarity gives

$$\nabla_\lambda \mathcal{L}(\lambda^*, \mu^*, \nu^*) = G^\top G\lambda^* - \mu^* + \nu^* \mathbf{1} = \mathbf{0}.$$

Since $G\lambda^* = g_{\text{mix}}$, the k -th component reads

$$\langle g_k, g_{\text{mix}} \rangle + \nu^* = \mu_k^*.$$

Complementary slackness gives $\mu_k^* \lambda_k^* = 0$. Thus, for $k \in \mathcal{A}$ we have $\lambda_k^* > 0$ and hence $\mu_k^* = 0$, implying $\langle g_k, g_{\text{mix}} \rangle = -\nu^*$ (a constant over $k \in \mathcal{A}$). For $k \notin \mathcal{A}$, $\mu_k^* \geq 0$ implies $\langle g_k, g_{\text{mix}} \rangle \geq -\nu^*$.

To identify the constant, multiply the stationarity equation by λ^* :

$$(\lambda^*)^\top G^\top G\lambda^* - (\lambda^*)^\top \mu^* + \nu^* (\lambda^*)^\top \mathbf{1} = 0.$$

We have $(\lambda^*)^\top G^\top G\lambda^* = \|G\lambda^*\|_2^2 = \|g_{\text{mix}}\|_2^2$, $(\lambda^*)^\top \mathbf{1} = 1$, and $(\lambda^*)^\top \mu^* = 0$ by complementary slackness. Hence $\|g_{\text{mix}}\|_2^2 + \nu^* = 0$, i.e., $-\nu^* = \|g_{\text{mix}}\|_2^2$. Substitute back to obtain $\langle g_k, g_{\text{mix}} \rangle \geq \|g_{\text{mix}}\|_2^2$ for all k , with equality for $k \in \mathcal{A}$. The supporting-face interpretation follows because the hyperplane $\{g : \langle g, g_{\text{mix}} \rangle = \|g_{\text{mix}}\|_2^2\}$ supports \mathcal{C} at the projection point g_{mix} . \square

A.7. Composite difficulty aggregation

Claim A.14 (Monotonicity and boundedness of the composite difficulty update). *Assume $\alpha, \beta \geq 0$ and define the instantaneous drive term $s_k := \alpha \overline{\text{RQ}}_k + \beta \overline{\text{Conf}}_k$. Then s_k is coordinatewise monotone in $(\overline{\text{RQ}}_k, \overline{\text{Conf}}_k)$, and the update*

$$D_k \leftarrow \text{clip}((1 - \rho)D_k + \rho s_k, [D_{\min}, D_{\max}])$$

ensures $D_k \in [D_{\min}, D_{\max}]$ for all time.

Proof. Monotonicity follows because s_k is an affine function with nonnegative coefficients. Boundedness follows from the definition of $\text{clip}(\cdot, [D_{\min}, D_{\max}])$, which maps any input to the closed interval $[D_{\min}, D_{\max}]$; thus by induction D_k always lies in that interval. \square

B. Log-Hypervolume Planning: Definitions and Proofs

This appendix provides formal definitions and proofs for Sec. 4.2. We consider a minimization setting throughout. Let $\tilde{\ell} = (\tilde{L}_1, \dots, \tilde{L}_K) \in \mathbb{R}^K$ denote the normalized loss vector and let $\mathbf{r} \in \mathbb{R}^K$ be a reference point satisfying $r_k > \tilde{L}_k$ for all k . (Note: we use ℓ for the loss vector to avoid confusion with the normalized Laplacian $\tilde{\mathbf{L}}$ from Sec. 4.1.)

B.1. Preliminaries: dominance and hypervolume

We first establish notation for Pareto dominance, then define the dominated hypervolume.

Definition B.1 (Dominance for minimization). For vectors $\mathbf{a}, \mathbf{b} \in \mathbb{R}^K$, we say \mathbf{a} *weakly dominates* \mathbf{b} (written $\mathbf{a} \preceq \mathbf{b}$) if $a_k \leq b_k$ for all $k \in \{1, \dots, K\}$. We say \mathbf{a} *strictly dominates* \mathbf{b} (written $\mathbf{a} \prec \mathbf{b}$) if $\mathbf{a} \preceq \mathbf{b}$ and $\mathbf{a} \neq \mathbf{b}$. For reference-point conditions, we write $\mathbf{r} \succ \tilde{\ell}$ to mean $r_k > \tilde{L}_k$ for all k (componentwise strict inequality).

Definition B.2 (Dominated hypervolume). Given a set of objective vectors $\mathcal{P} \subset \mathbb{R}^K$ and a reference point \mathbf{r} , the dominated region is

$$\mathcal{Z}(\mathcal{P}, \mathbf{r}) := \{z \in \mathbb{R}^K : \exists y \in \mathcal{P} \text{ such that } y \preceq z \preceq \mathbf{r}\},$$

and the hypervolume indicator is the K -dimensional Lebesgue measure $\text{HV}(\mathcal{P}, \mathbf{r}) := \text{Vol}(\mathcal{Z}(\mathcal{P}, \mathbf{r}))$.

Claim B.3 (Singleton reduction). *If $\mathcal{P} = \{\tilde{\ell}\}$ is a singleton and $\mathbf{r} \succ \tilde{\ell}$ coordinatewise, then*

$$\text{HV}(\{\tilde{\ell}\}, \mathbf{r}) = \prod_{k=1}^K (r_k - \tilde{L}_k).$$

Proof. For a singleton, the dominated region is exactly the axis-aligned hyperrectangle $\mathcal{Z}(\{\tilde{\ell}\}, \mathbf{r}) = \{z \in \mathbb{R}^K : \tilde{L}_k \leq z_k \leq r_k \forall k\}$. Its Lebesgue measure is the product of side lengths, giving the stated expression. \square

B.2. Pareto compliance for fixed reference point

The key property we require is that strict Pareto improvements yield strict increases in the planning signal.

Theorem B.4 (Singleton HV is strictly Pareto-compliant). *Fix a reference point \mathbf{r} such that $r_k > a_k$ and $r_k > b_k$ for all k . If \mathbf{a} strictly dominates \mathbf{b} (Definition B.1), then $\text{HV}(\{\mathbf{a}\}, \mathbf{r}) > \text{HV}(\{\mathbf{b}\}, \mathbf{r})$.*

Proof. By Claim B.3, we have $\text{HV}(\{\mathbf{a}\}, \mathbf{r}) = \prod_{k=1}^K (r_k - a_k)$ and similarly for \mathbf{b} . Since $\mathbf{a} \prec \mathbf{b}$, each factor satisfies $r_k - a_k \geq r_k - b_k \geq 0$. Moreover, $\mathbf{a} \neq \mathbf{b}$ implies strict inequality $r_j - a_j > r_j - b_j$ for at least one index j . Since all factors are strictly positive (by the reference-point condition), the product over k is strictly larger for \mathbf{a} than for \mathbf{b} . \square

Corollary B.5 (Log-HV is also Pareto-compliant (fixed \mathbf{r})). *Under the conditions of Theorem B.4, $\phi(\mathbf{x}) := \sum_{k=1}^K \log(r_k - x_k)$ satisfies $\phi(\mathbf{a}) > \phi(\mathbf{b})$.*

Proof. $\log(\cdot)$ is strictly increasing on $\mathbb{R}_{>0}$, so $\log \text{HV}(\{\mathbf{a}\}, \mathbf{r}) > \log \text{HV}(\{\mathbf{b}\}, \mathbf{r})$. Using Claim B.3 gives $\log \text{HV}(\{\mathbf{x}\}, \mathbf{r}) = \sum_k \log(r_k - x_k)$. \square

B.3. Log-hypervolume sensitivities

Claim B.6 (Gradient of log-HV and the sensitivity weight). *Fix \mathbf{r} and define $\phi(\tilde{\ell}) = \sum_{k=1}^K \log(r_k - \tilde{L}_k)$. Then for each k ,*

$$\frac{\partial \phi}{\partial \tilde{L}_k} = -\frac{1}{r_k - \tilde{L}_k}.$$

Consequently, the sensitivity magnitude used in Sec. 4.2,

$$w_k^{\text{HV}} := \frac{1}{r_k - \tilde{L}_k + \varepsilon},$$

is a stabilized version of $-\partial \phi / \partial \tilde{L}_k$.

Proof. The function ϕ is separable across coordinates. Differentiating $\log(r_k - \tilde{L}_k)$ w.r.t. \tilde{L}_k yields $\partial/\partial\tilde{L}_k \log(r_k - \tilde{L}_k) = -(r_k - \tilde{L}_k)^{-1}$. All other terms do not depend on \tilde{L}_k . \square

Claim B.7 (Relation to the HV gradient). *Let $\text{HV}(\tilde{\ell}) = \prod_k (r_k - \tilde{L}_k)$ with fixed \mathbf{r} . Then*

$$\frac{\partial \text{HV}}{\partial \tilde{L}_k} = -\frac{\text{HV}(\tilde{\ell})}{r_k - \tilde{L}_k}, \quad \frac{\partial \log \text{HV}}{\partial \tilde{L}_k} = -\frac{1}{r_k - \tilde{L}_k}.$$

Proof. Differentiate the product: $\partial \text{HV} / \partial \tilde{L}_k = -\prod_{j \neq k} (r_j - \tilde{L}_j)$, and note that $\prod_{j \neq k} (r_j - \tilde{L}_j) = \text{HV} / (r_k - \tilde{L}_k)$. The second identity follows from Claim B.6 and $\log \text{HV} = \sum_k \log(r_k - \tilde{L}_k)$. \square

Remark B.8 (Why log-HV sensitivities are preferred). Claim B.7 reveals a key difference: the HV gradient at coordinate k scales with the current hypervolume value, whereas the log-HV gradient depends only on the slack $(r_k - \tilde{L}_k)$. Using log-HV sensitivities therefore yields priorities that are invariant to the absolute scale of the dominated region, making them more stable across training phases where HV may span orders of magnitude.

B.4. Reference point specification and positivity

Claim B.9 (Positivity condition for log-HV). *$\phi(\tilde{\ell}) = \sum_k \log(r_k - \tilde{L}_k)$ is well-defined if and only if $r_k - \tilde{L}_k > 0$ for all k .*

Proof. Each term $\log(r_k - \tilde{L}_k)$ is defined if and only if its argument is positive. The claim follows by separability. \square

Remark B.10 (Reference point initialization). To guarantee positivity throughout training, we initialize r_k from a short warm-up window observed on the full graph: $r_k \leftarrow (1 + \delta) \max_{t \leq t_{\text{warm}}} \tilde{L}_k(t)$. We also apply a monotone safeguard $r_k \leftarrow \max(r_k, \tilde{L}_k + \delta)$ to handle rare upward fluctuations. Since HV values depend on \mathbf{r} , we treat log-HV as a priority signal for planning rather than a globally comparable metric across time.

B.5. Deriving the allocation plan

Sec. 4.2 converts per-objective planning priorities into an allocation fraction $f \in \Delta^K$. Let

$$a_k := \frac{w_k^{\text{HV}}}{1 + \gamma D_k},$$

which we interpret as a difficulty-adjusted marginal value score (higher is better).

Proposition B.11 (Proportional-fair allocation yields normalized priorities). *Consider the concave planning objective*

$$\max_{f \in \Delta^K, f \succ 0} \sum_{k=1}^K a_k \log f_k.$$

Its unique maximizer is $f_k^ = a_k / \sum_{j=1}^K a_j$, which matches Eq. (7) in Sec. 4.2.*

Proof. Form the Lagrangian $\mathcal{L}(f, \nu) = \sum_k a_k \log f_k + \nu(1 - \sum_k f_k)$. Stationarity gives $\partial \mathcal{L} / \partial f_k = a_k / f_k - \nu = 0$, so $f_k = a_k / \nu$. Enforcing $\sum_k f_k = 1$ yields $\nu = \sum_j a_j$, hence $f_k^* = a_k / \sum_j a_j$. Strict concavity of $\sum_k a_k \log f_k$ on $f \succ 0$ implies uniqueness. \square

Remark B.12 (Interpretation of the proportional-fair planner). Proposition B.11 provides a principled rationale for converting priorities into a non-degenerate allocation over tasks: it favors high-priority tasks while avoiding collapsing all budget onto a single objective. Other regularizers (e.g., entropy or minimum-floor constraints) can be incorporated via standard convex analysis; we evaluate these variants in ablations.

C. Tactical Execution: Deficit Dynamics and Guarantees

This appendix formalizes the controller in Sec. 4.3. We fix an epoch t and suppress (t) in $f_k(t)$ for readability.

C.1. Deficit dynamics and basic identities

Definition C.1 (Counts, reference, and pre-decision deficits). Let $f \in \Delta^K$ be fixed within an epoch. Let $N_k(m) := \sum_{\tau=1}^m \mathbb{1}\{k_{t,\tau} = k\}$ be realized counts after m executed blocks, and let $N_k^{\text{ref}}(m) := mf_k$ be the reference trajectory. Define the pre-decision deficit at block m as

$$e_k(m) := N_k^{\text{ref}}(m) - N_k(m-1) = mf_k - N_k(m-1).$$

Claim C.2 (Sum of deficits is constant). *For every $m \geq 1$, $\sum_{k=1}^K e_k(m) = 1$.*

Proof. We have

$$\sum_{k=1}^K e_k(m) = \sum_{k=1}^K (mf_k - N_k(m-1)) = m \sum_{k=1}^K f_k - \sum_{k=1}^K N_k(m-1).$$

Because $f \in \Delta^K$, $\sum_k f_k = 1$, and because exactly one task is selected per block, $\sum_k N_k(m-1) = m-1$. Hence $\sum_k e_k(m) = m - (m-1) = 1$. \square

Claim C.3 (Deficit recursion). *Let $k_{t,m}$ be the task executed at block m . Then for every k and $m \geq 1$,*

$$e_k(m+1) = e_k(m) + f_k - \mathbb{1}\{k_{t,m} = k\}.$$

Proof. By definition,

$$e_k(m+1) = (m+1)f_k - N_k(m) = mf_k - N_k(m-1) + f_k - (N_k(m) - N_k(m-1)).$$

The increment $N_k(m) - N_k(m-1)$ equals $\mathbb{1}\{k_{t,m} = k\}$, giving the recursion. \square

C.2. A worst-case tracking guarantee in the max-deficit limit

The following result provides a clean, worst-case tracking guarantee for a canonical deterministic controller. It is the discrete analogue of deficit/credit-based fair schedulers.

Definition C.4 (Max-deficit controller). At each block m , choose

$$k_{t,m} \in \arg \max_{k \in [K]} e_k(m).$$

(Ties may be broken arbitrarily.)

Theorem C.5 (Uniform $O(1)$ tracking error under max-deficit scheduling). *Define the post-execution discrepancy*

$$d_k(m) := N_k(m) - mf_k.$$

Under the max-deficit controller (Def. C.4), for every $m \geq 0$ and every $k \in [K]$,

$$-1 < d_k(m) < 1.$$

Proof. We proceed in two parts.

(Upper bound: $d_k(m) < 1$). We prove by induction on m . The base case $m = 0$ satisfies $d_k(0) = 0 < 1$. Assume $d_k(m-1) < 1$ for all k .

If task k is not chosen at block m , then $N_k(m) = N_k(m-1)$ and

$$\begin{aligned} d_k(m) &= N_k(m-1) - mf_k = (N_k(m-1) - (m-1)f_k) - f_k \\ &= d_k(m-1) - f_k < d_k(m-1) < 1. \end{aligned}$$

If task k is chosen at block m , then $N_k(m) = N_k(m-1) + 1$ and

$$d_k(m) = N_k(m-1) + 1 - mf_k = d_k(m-1) + 1 - f_k.$$

To show this is < 1 , we use the selection rule. Note that

$$e_k(m) = mf_k - N_k(m-1) = f_k - d_k(m-1).$$

By Claim C.2, $\sum_j e_j(m) = 1$, hence $\max_j e_j(m) \geq 1/K > 0$. Since k is chosen among maximizers, $e_k(m) > 0$, implying $d_k(m-1) < f_k$. Therefore

$$d_k(m) = d_k(m-1) + 1 - f_k < f_k + 1 - f_k = 1.$$

(Lower bound: $d_k(m) > -1$). Assume for contradiction that there exists a first time $m \geq 1$ and an index j such that $d_j(m) \leq -1$. Consider block m .

If j is chosen at block m , then $d_j(m) = d_j(m-1) + 1 - f_j > -1 + 1 - f_j = -f_j \geq -1$, contradicting $d_j(m) \leq -1$. Thus j is not chosen at block m , so $d_j(m) = d_j(m-1) - f_j \leq -1$, i.e.,

$$d_j(m-1) \leq -1 + f_j.$$

Then the deficit satisfies

$$e_j(m) = f_j - d_j(m-1) \geq f_j - (-1 + f_j) = 1.$$

But Claim C.2 gives $\sum_k e_k(m) = 1$, so $e_j(m) \geq 1$ forces $e_j(m) = \max_k e_k(m)$, and the max-deficit controller must choose j at block m , a contradiction. Therefore no such m exists and $d_k(m) > -1$ for all k, m .

Combining upper and lower bounds yields the claim. \square

C.3. Relation to the PID-softmax controller

Claim C.6 (Softmax concentrates on argmax as temperature vanishes). *Fix $u \in \mathbb{R}^K$ and define $q_\tau = \text{softmax}(u/\tau)$ with $\tau > 0$. Let $\mathcal{A} = \arg \max_k u_k$. Then as $\tau \downarrow 0$, q_τ assigns probability mass only to \mathcal{A} , and for any $i \notin \mathcal{A}$, $q_{\tau,i} \rightarrow 0$.*

Proof. Let $u^* = \max_k u_k$. For any i ,

$$q_{\tau,i} = \frac{e^{u_i/\tau}}{\sum_j e^{u_j/\tau}} = \frac{e^{(u_i - u^*)/\tau}}{\sum_j e^{(u_j - u^*)/\tau}}.$$

If $i \notin \mathcal{A}$ then $u_i - u^* < 0$, so $e^{(u_i - u^*)/\tau} \rightarrow 0$ as $\tau \downarrow 0$, while for $j \in \mathcal{A}$ the exponent is 0 and the corresponding terms remain 1. Hence $q_{\tau,i} \rightarrow 0$ for $i \notin \mathcal{A}$ and total mass concentrates on \mathcal{A} . \square

Remark C.7 (Max-deficit as a limiting case of PID-softmax). If $K_I^{(k)} = K_D^{(k)} = 0$, $\epsilon = 0$, and $\nu_k(m) = K_P e_k(m)$, then $\arg \max_k \nu_k(m) = \arg \max_k e_k(m)$ and by Claim C.6 the sampling rule in Eq. (11) approaches the deterministic max-deficit controller as $\tau \downarrow 0$.

C.4. Starvation prevention under explicit exploration

Claim C.8 (Uniform lower bound on per-step selection probability). *Under Eq. (11), for every m and every k , $p_k(m) \geq \epsilon/K$.*

Proof. Eq. (11) is a convex combination of two distributions: $(1 - \epsilon)$ softmax(\cdot) and $\epsilon \cdot \mathbf{1}/K$. Therefore each coordinate is at least ϵ/K . \square

Proposition C.9 (Geometric tail bound on drought length). *Fix any task k and any time m_0 . Let T be the first time $m \geq m_0$ such that $k_{t,m} = k$. Then for any integer $s \geq 1$,*

$$\Pr(T > m_0 + s \mid \mathcal{F}_{m_0}) \leq \left(1 - \frac{\epsilon}{K}\right)^s,$$

where \mathcal{F}_{m_0} is the sigma-field generated by the history up to time m_0 .

Proof. By Claim C.8, for every $m \geq m_0$ we have

$$\Pr(k_{t,m} \neq k \mid \mathcal{F}_{m-1}) = 1 - p_k(m) \leq 1 - \epsilon/K.$$

Therefore, using the chain rule for conditional probabilities,

$$\begin{aligned} \Pr(T > m_0 + s \mid \mathcal{F}_{m_0}) &= \Pr\left(\bigcap_{r=1}^s \{k_{t,m_0+r} \neq k\} \mid \mathcal{F}_{m_0}\right) \\ &= \prod_{r=1}^s \Pr(k_{t,m_0+r} \neq k \mid \mathcal{F}_{m_0+r-1}) \\ &\leq \left(1 - \frac{\epsilon}{K}\right)^s. \end{aligned}$$

□

Corollary C.10 (Bound on expected waiting time). *Under the conditions of Prop. C.9, $\mathbb{E}[T - m_0 \mid \mathcal{F}_{m_0}] \leq K/\epsilon$.*

Proof. A nonnegative integer-valued random variable satisfies $\mathbb{E}[X] = \sum_{s \geq 0} \Pr(X > s)$. Apply Prop. C.9 with $X = T - m_0$:

$$\begin{aligned} \mathbb{E}[T - m_0 \mid \mathcal{F}_{m_0}] &= \sum_{s \geq 0} \Pr(T > m_0 + s \mid \mathcal{F}_{m_0}) \\ &\leq \sum_{s \geq 0} \left(1 - \frac{\epsilon}{K}\right)^s = \frac{K}{\epsilon}. \end{aligned}$$

□

C.5. Implementation stabilizers

Claim C.11 (Anti-windup by clipping keeps the integral state bounded). *If the integrator update is implemented as*

$$I_k(m) \leftarrow \text{clip}\left(I_k(m-1) + e_k(m), [-I_{\max}, I_{\max}]\right),$$

then $|I_k(m)| \leq I_{\max}$ for all m .

Proof. Immediate from the definition of $\text{clip}(\cdot, [-I_{\max}, I_{\max}])$. □

Remark C.12 (Why anti-windup is necessary). When the controller output is effectively saturated (here, logits/probabilities cannot instantaneously realize arbitrary reference changes), the integral term can accumulate persistent error and degrade responsiveness. Clipping (or back-calculation) is a standard anti-windup safeguard in PID control.

D. Additional Experimental Details

D.1. Pretext task objectives

Let $G = (V, E, X)$ be a graph with $|V| = n$ nodes, adjacency A , and node features $X \in \mathbb{R}^{n \times d_x}$. The encoder f_θ maps the graph (or an augmented view of it) to node embeddings $Z = f_\theta(G) \in \mathbb{R}^{n \times d}$, with row vector $z_v \in \mathbb{R}^d$ for node v . Unless otherwise stated, objectives are estimated on minibatches (or sampled subgraphs) but are defined below at the population level for clarity.

(p_link) Link prediction (LP). We train a decoder $s_\phi(z_u, z_v)$ (e.g., dot-product or an MLP) to predict whether an edge exists between node pairs. Let E^+ denote observed (positive) edges and E^- denote sampled non-edges (negative pairs). The link prediction objective is a binary cross-entropy loss:

$$\mathcal{L}_{\text{LP}}(\theta, \phi) = -\frac{1}{|E^+|} \sum_{(u,v) \in E^+} \log \sigma(s_\phi(z_u, z_v)) - \frac{1}{|E^-|} \sum_{(u,v) \in E^-} \log(1 - \sigma(s_\phi(z_u, z_v))), \quad (12)$$

where $\sigma(\cdot)$ is the logistic sigmoid. When downstream evaluation includes link prediction, we compute \mathcal{L}_{LP} on the *training* graph only (validation/test edges removed) to prevent leakage.

(p_recon) Masked feature reconstruction (MFR). We randomly mask a subset of nodes (or features) and train the model to reconstruct the original attributes. Let $m \in \{0, 1\}^n$ indicate which nodes are masked and let $\tilde{X} = \text{Mask}(X; m)$ denote corrupted features (e.g., replaced by a mask token or zeros). We encode the corrupted graph to get $\tilde{Z} = f_\theta(G, \tilde{X})$ and decode features with g_ψ : $\hat{X} = g_\psi(\tilde{Z})$. We reconstruct only masked entries:

$$\mathcal{L}_{\text{MFR}}(\theta, \psi) = \frac{1}{\sum_v m_v} \sum_{v \in V: m_v=1} \ell_{\text{rec}}(\hat{x}_v, x_v), \quad (13)$$

where ℓ_{rec} is a reconstruction loss (e.g., MSE for continuous features, or cross-entropy for one-hot features). The masking ratio and ℓ_{rec} choice are reported in App. D.4.

(p_minsg) Mutual-information node–subgraph contrast (MI-NSG). This objective encourages agreement between an anchor node representation and a summary of its local subgraph context under stochastic augmentations. We generate two augmented views $G^{(1)} = \text{Aug}(G)$ and $G^{(2)} = \text{Aug}(G)$ (e.g., feature/edge dropout). Let $Z^{(1)} = f_\theta(G^{(1)})$ and $Z^{(2)} = f_\theta(G^{(2)})$. For each node v , define a local subgraph summary (context) vector

$$c_v^{(2)} = \text{READOUT}(\{z_u^{(2)} : u \in \mathcal{S}(v)\}), \quad (14)$$

where $\mathcal{S}(v)$ denotes the nodes in v 's local neighborhood/subgraph (e.g., r -hop ego graph) and READOUT is a permutation-invariant pooling operator. We then optimize an InfoNCE-style contrastive objective between $z_v^{(1)}$ and its matched context $c_v^{(2)}$:

$$\mathcal{L}_{\text{MI-NSG}}(\theta) = -\frac{1}{n} \sum_{v \in V} \log \frac{\exp(\text{sim}(z_v^{(1)}, c_v^{(2)})/\tau)}{\sum_{u \in V} \exp(\text{sim}(z_v^{(1)}, c_u^{(2)})/\tau)}, \quad (15)$$

where $\text{sim}(\cdot, \cdot)$ is a similarity function (e.g., dot product or cosine) and τ is a temperature. Augmentation choices and τ are reported in App. D.4.

(p_decor) Representation decorrelation (RepDecor). RepDecor reduces redundancy between embedding dimensions using a Barlow-Twins-style objective. Using two augmented views as above, we obtain embeddings for a minibatch of nodes $\mathcal{B} \subseteq V$ and a projection head h : $Y^{(1)} = \text{Norm}(h(Z_{\mathcal{B}}^{(1)}))$ and $Y^{(2)} = \text{Norm}(h(Z_{\mathcal{B}}^{(2)}))$. Let $C \in \mathbb{R}^{d \times d}$ be the cross-correlation matrix:

$$C_{ij} = \frac{1}{|\mathcal{B}|} \sum_{v \in \mathcal{B}} Y_{v,i}^{(1)} Y_{v,j}^{(2)}. \quad (16)$$

The RepDecor objective encourages C to approach the identity:

$$\mathcal{L}_{\text{Decor}}(\theta) = \sum_i (1 - C_{ii})^2 + \lambda \sum_{i \neq j} C_{ij}^2, \quad (17)$$

where $\lambda > 0$ controls the strength of redundancy reduction. We report λ and whether a projection head is used in App. D.4.

(p_par) Partition prediction (PAR). We compute a K_{par} -way partition of the training graph using METIS and treat the partition IDs as pseudo-labels. Let $y_v \in \{1, \dots, K_{\text{par}}\}$ denote the partition assignment and let $q_\omega(\cdot | z_v)$ be a classifier head producing logits over partitions. We minimize the cross-entropy:

$$\mathcal{L}_{\text{PAR}}(\theta, \omega) = -\frac{1}{n} \sum_{v \in V} \log \left(\text{softmax}(q_\omega(z_v)) \right)_{y_v}. \quad (18)$$

Unless stated otherwise, partitions are computed once per dataset (on the training graph) and kept fixed during pretraining; K_{par} is listed in App. D.4.

D.2. Dataset statistics and preprocessing

Table 3 summarizes dataset sizes (nodes, edges, features, classes), split protocols, and any preprocessing steps used in our pipeline.

Table 3. Dataset statistics for the 9-dataset benchmark.

Dataset	Nodes	Edges	Features	Classes	Homophily	Type
Chameleon (Rozemberczki et al., 2019)	2,277	31,371	2,325	5	0.23	wikipedia
Cora (Yang et al., 2016)	2,708	5,278	1,433	7	0.81	citation
CiteSeer (Yang et al., 2016)	3,327	4,552	3,703	6	0.74	citation
Squirrel (Rozemberczki et al., 2019)	5,201	198,353	2,089	5	0.22	wikipedia
Actor (Pei et al., 2020)	7,600	26,659	932	5	0.22	actor
Wiki-CS (Mernyei & Cangea, 2020)	11,701	216,123	300	10	0.65	wikipedia
Coauthor-CS (Shchur et al., 2018)	18,333	81,894	6,805	15	0.81	coauthor
PubMed (Yang et al., 2016)	19,717	44,324	500	3	0.80	citation
ogbn-arxiv (Hu et al., 2020)	169,343	1,166,243	128	40	0.66	citation

D.3. Evaluation protocols

We describe downstream evaluation in detail, including: (i) linear probing for node classification (optimizer, regularization, early stopping, split usage), (ii) link prediction protocol (edge splits, negative sampling, decoder architecture, metrics), and (iii) clustering evaluation (K-means configuration, number of restarts, metric computation). All evaluations use a frozen encoder and are repeated across seeds.

D.4. Hyperparameters and reproducibility

To ensure fair comparisons, all methods use the same dataset-specific step budget and the same backbone family. Table 4 lists the hyperparameter search grids shared across methods, while Table 5 reports the selected hyperparameters per dataset for ControlG.

Table 4. Hyperparameter search grids. Values in {braces} indicate discrete choices.

Method	Parameter	Search Space
ControlG	K_p	{0.5, 1.0, 2.0}
	K_i	{0.05, 0.1}
	K_d	{0.0, 0.1}
	ϵ	{0.05, 0.1}
	f_{\min}	{0.05, 0.1}
	γ	{0.5, 1.0}
	block_size	{1, 2}
	sense_period	{5, 10}
	β	{0.25, 0.5}
AutoSSL (Jin et al., 2021)	lr_lambda	{0.01, 0.05, 0.1}
	meta_every	{5, 10, 20}
	meta_warmup_steps	{0, 50}
	lr	{0.0005, 0.001, 0.005}
WAS (Fan et al., 2024)	ema_beta	{0.8, 0.9, 0.95}
	select_temperature	{0.5, 1.0, 2.0}
	select_ll	{0.0, 0.001, 0.01}
	lr	{0.0005, 0.001, 0.005}
ParetoGNN (Ju et al., 2022)	use_pareto	{True, False}
	grad_norm	{l2, none}
	lr	{0.0005, 0.001, 0.005}
PCGrad (Yu et al., 2020)	reduction	{mean, sum}
	lr	{0.0005, 0.001, 0.005}
CAGrad (Liu et al., 2021)	c	{0.2, 0.4, 0.5, 0.6, 0.8}
	max_iter	{20, 50, 100}
	lr	{0.0005, 0.001, 0.005}

Table 5. Selected hyperparameters for ControlG per dataset after grid search.

Dataset	K_p	K_i	K_d	ϵ	f_{\min}	γ	Block	Sense	β	LR	Hidden
Cora	0.5	0.1	0.1	0.05	0.1	1.0	1	10	0.25	0.001	512
CiteSeer	1.0	0.05	0.1	0.1	0.1	1.0	2	10	0.5	0.0001	512
Chameleon	2.0	0.1	0.1	0.05	0.1	0.5	1	5	0.5	0.01	256
Squirrel	0.5	0.05	0.0	0.1	0.1	0.5	1	10	0.25	0.001	512
Actor	0.5	0.05	0.0	0.1	0.05	1.0	1	5	0.25	0.0003	128
PubMed	2.0	0.1	0.1	0.1	0.1	0.5	1	5	0.5	0.003	256
Wiki-CS	1.0	0.1	0.1	0.1	0.1	1.0	1	10	0.5	0.0003	256
Coauthor-CS	1.0	0.1	0.0	0.05	0.1	0.5	2	10	0.25	0.003	512
ogbn-arxiv	2.0	0.5	0.1	0.2	0.0	0.5	10	10	0.25	0.0003	256

D.5. Additional results: link prediction

Table 6 reports link prediction performance (AUC) across datasets. We place this table in the appendix due to space constraints in the main text.

Method	Cora	CiteSeer	Chameleon	Squirrel	Actor	PubMed	Wiki-CS	Co-CS	Avg Rank
BGRL	90.18 ± 1.5	85.26 ± 2.5	87.53 ± 3.7	54.09 ± 1.4	62.01 ± 2.2	94.04 ± 0.2	95.01 ± 0.2	95.13 ± 0.2	11.4
DGI	83.62 ± 1.2	88.74 ± 0.8	90.27 ± 0.5	89.82 ± 0.3	70.04 ± 1.1	88.71 ± 0.8	86.80 ± 1.0	94.51 ± 0.1	10.6
GRACE	82.69 ± 1.5	90.02 ± 0.4	86.20 ± 3.0	93.39 ± 1.5	80.65 ± 0.4	90.23 ± 0.3	95.08 ± 0.2	93.87 ± 1.4	7.0
MVGRL	88.39 ± 1.1	79.00 ± 3.6	90.63 ± 0.5	—	57.51 ± 1.7	86.57 ± 0.9	—	89.97 ± 1.3	12.5
p_link	90.38 ± 0.4	89.37 ± 0.5	95.62 ± 0.1	91.36 ± 1.6	68.35 ± 0.2	95.63 ± 0.1	91.99 ± 0.5	94.26 ± 0.0	7.9
p_recon	91.46 ± 0.3	92.50 ± 0.5	72.40 ± 5.8	85.16 ± 0.6	54.07 ± 0.8	92.24 ± 0.7	94.76 ± 0.4	95.96 ± 0.1	10.4
p_minsg	91.16 ± 0.2	95.13 ± 0.3	92.89 ± 0.6	89.97 ± 0.3	59.69 ± 0.8	93.78 ± 0.5	94.99 ± 0.1	96.24 ± 0.2	8.1
p_decor	51.56 ± 3.6	55.93 ± 1.6	85.13 ± 1.5	89.83 ± 0.3	52.36 ± 1.7	90.84 ± 0.3	78.56 ± 3.3	88.30 ± 1.0	14.1
p_par	92.26 ± 1.6	95.22 ± 0.4	87.17 ± 3.1	89.02 ± 0.4	71.54 ± 0.4	83.48 ± 1.0	92.74 ± 0.3	87.72 ± 1.3	10.0
AutoSSL	96.30 ± 0.2	96.56 ± 0.5	95.68 ± 1.0	91.89 ± 2.1	65.45 ± 1.6	91.12 ± 0.7	92.14 ± 0.9	94.13 ± 0.9	6.8
WAS	93.73 ± 1.6	95.78 ± 3.5	91.48 ± 2.4	89.57 ± 2.7	77.92 ± 2.7	94.15 ± 1.9	91.49 ± 2.1	92.67 ± 1.5	9.0
Uniform	96.28 ± 0.1	98.17 ± 0.0	96.39 ± 0.2	90.46 ± 0.4	64.83 ± 0.2	96.39 ± 0.0	93.23 ± 0.6	97.52 ± 0.1	4.4
ParetoGNN	95.73 ± 0.2	98.20 ± 0.1	96.15 ± 0.3	91.31 ± 0.8	69.18 ± 0.7	77.46 ± 3.8	95.57 ± 0.1	97.11 ± 0.1	5.6
PCGrad	93.57 ± 0.6	98.20 ± 0.1	96.28 ± 0.2	89.23 ± 0.4	70.28 ± 0.2	96.38 ± 0.0	95.99 ± 0.1	94.50 ± 0.5	5.0
CAGrad	95.32 ± 0.2	97.93 ± 0.0	95.57 ± 0.2	90.15 ± 0.8	72.01 ± 0.2	96.17 ± 0.1	93.66 ± 0.4	93.64 ± 0.3	6.5
Random	95.77 ± 0.4	97.77 ± 0.4	95.60 ± 0.3	94.23 ± 0.8	67.22 ± 1.0	92.56 ± 1.2	93.66 ± 1.6	94.04 ± 2.0	6.1
Round-Robin	95.02 ± 0.4	98.23 ± 0.1	95.80 ± 0.3	90.93 ± 0.2	78.77 ± 0.6	94.62 ± 0.1	94.23 ± 0.1	97.96 ± 0.0	4.1
ControlG	97.42 ± 0.2	99.24 ± 0.1	96.32 ± 0.4	93.12 ± 0.1	78.42 ± 0.5	97.48 ± 0.1	95.72 ± 0.1	97.68 ± 0.1	1.9

Table 6. Link prediction AUC. Mean \pm 95% CI over 5 seeds. First, second, and third best methods per dataset are highlighted. Avg Rank is the mean rank across datasets (lower is better). ControlG achieves the best average rank with strong performance on both homophilic and heterophilic graphs.

D.6. Additional results: node clustering

Table 7 reports node clustering performance (NMI) across datasets. We place this table in the appendix due to space constraints.

D.7. Ablations

We report component ablations that remove (i) spectral demand, (ii) interference, (iii) the planner, and (iv) the controller/tracking mechanism. Table 8 shows ablation results for link prediction (the node classification ablation is in the main text, Table 2).

D.8. Compute and overhead

We report wall-clock overhead decompositions (sensing, planning, control) and time-to-accuracy curves for representative datasets. This section supports the claim that ControlG is practical and that its additional computation is concentrated in

Method	Cora	CiteSeer	Chameleon	Squirrel	Actor	PubMed	Wiki-CS	Co-CS	Avg Rank
BGRL	46.24 \pm 4.1	3.81 \pm 0.2	6.44 \pm 0.7	1.32 \pm 0.0	0.86 \pm 0.2	19.84 \pm 2.0	35.65 \pm 0.9	36.11 \pm 3.5	11.4
DGI	43.88 \pm 4.6	35.35 \pm 2.8	15.14 \pm 2.4	3.03 \pm 0.2	1.10 \pm 0.3	25.92 \pm 6.8	6.89 \pm 2.4	70.92 \pm 1.8	5.8
GRACE	16.07 \pm 2.0	12.91 \pm 3.7	6.41 \pm 0.9	3.47 \pm 0.6	1.33 \pm 0.2	15.57 \pm 2.4	35.68 \pm 0.3	58.22 \pm 7.1	9.4
MVGRL	48.57 \pm 3.7	22.06 \pm 4.4	10.83 \pm 1.2	—	5.21 \pm 0.3	21.27 \pm 6.0	—	56.89 \pm 8.9	6.5
p_link	26.87 \pm 1.3	21.84 \pm 1.8	8.82 \pm 0.6	2.99 \pm 0.5	1.39 \pm 0.0	11.55 \pm 0.0	27.73 \pm 0.5	59.38 \pm 1.5	10.9
p_recon	40.82 \pm 3.0	18.26 \pm 4.3	3.64 \pm 1.3	1.11 \pm 0.1	2.31 \pm 0.2	5.69 \pm 1.4	30.39 \pm 1.5	65.53 \pm 3.1	10.1
p_minsg	15.05 \pm 2.2	25.35 \pm 2.6	8.72 \pm 1.2	2.94 \pm 0.8	2.24 \pm 0.3	24.85 \pm 6.5	33.13 \pm 1.6	64.72 \pm 2.0	9.0
p_decor	9.20 \pm 4.3	2.01 \pm 0.8	12.55 \pm 0.4	3.56 \pm 0.0	0.40 \pm 0.1	22.65 \pm 0.6	24.80 \pm 5.6	54.04 \pm 1.4	10.5
p_par	35.20 \pm 1.7	15.53 \pm 1.8	6.58 \pm 2.2	2.41 \pm 0.4	0.95 \pm 0.1	29.12 \pm 1.8	31.79 \pm 0.3	54.48 \pm 1.0	10.4
AutoSSL	46.00 \pm 3.6	32.54 \pm 4.8	6.26 \pm 1.4	1.82 \pm 0.4	2.32 \pm 0.1	15.62 \pm 7.2	35.75 \pm 0.3	62.40 \pm 4.3	7.3
WAS	36.46 \pm 5.1	18.96 \pm 3.0	8.53 \pm 1.7	3.24 \pm 0.6	1.34 \pm 0.7	26.84 \pm 6.5	29.43 \pm 1.5	53.98 \pm 1.6	10.0
Uniform	37.98 \pm 1.8	19.00 \pm 0.6	11.06 \pm 2.2	1.96 \pm 0.3	1.78 \pm 0.3	29.19 \pm 2.6	35.55 \pm 2.0	66.10 \pm 1.6	6.9
ParetoGNN	44.61 \pm 0.9	18.83 \pm 2.3	7.33 \pm 1.2	2.96 \pm 0.7	1.11 \pm 0.4	18.69 \pm 6.3	39.62 \pm 1.0	64.18 \pm 1.0	8.1
PCGrad	44.29 \pm 2.5	19.08 \pm 1.5	8.40 \pm 1.8	1.98 \pm 0.2	1.65 \pm 0.2	26.82 \pm 0.4	38.17 \pm 0.7	63.52 \pm 0.5	7.8
CAGrad	46.56 \pm 3.0	28.63 \pm 1.9	5.48 \pm 1.0	2.41 \pm 0.3	0.78 \pm 0.1	19.33 \pm 0.5	35.45 \pm 2.2	58.50 \pm 1.4	8.4
Random	45.36 \pm 2.4	18.39 \pm 2.5	9.63 \pm 0.2	4.57 \pm 0.4	1.82 \pm 0.3	29.95 \pm 1.1	39.68 \pm 1.3	63.07 \pm 3.3	5.0
Round-Robin	38.23 \pm 2.1	21.83 \pm 2.7	12.22 \pm 1.0	2.83 \pm 0.2	0.70 \pm 0.4	29.37 \pm 1.8	40.25 \pm 1.2	65.98 \pm 0.6	5.1
ControlG	50.12 \pm 2.8	34.12 \pm 2.1	14.36 \pm 1.8	4.28 \pm 0.3	4.86 \pm 0.4	31.42 \pm 1.4	40.08 \pm 0.8	68.24 \pm 1.2	1.8

Table 7. **Node clustering (NMI \times 100).** Mean \pm 95% CI over 5 seeds. First, second, and third best methods per dataset are highlighted. **Avg Rank** is the mean rank across datasets (lower is better). ControlG achieves the best average rank with consistent top-tier clustering quality.

Variant	Cora	CiteSeer	Chameleon	Squirrel	Actor	PubMed	Wiki-CS	Co-CS
ControlG (full)	97.42 \pm 0.2	99.24 \pm 0.1	96.32 \pm 0.4	93.12 \pm 0.1	78.42 \pm 0.5	97.48 \pm 0.1	95.72 \pm 0.1	97.68 \pm 0.1
w/o spectral demand ($\alpha=0$)	96.58 \pm 0.3	98.56 \pm 0.2	95.24 \pm 0.5	91.86 \pm 0.2	77.14 \pm 0.6	96.52 \pm 0.2	94.68 \pm 0.2	96.84 \pm 0.2
w/o interference ($\beta=0$)	96.94 \pm 0.2	98.82 \pm 0.1	95.68 \pm 0.4	92.34 \pm 0.2	77.58 \pm 0.5	97.02 \pm 0.1	95.18 \pm 0.1	97.24 \pm 0.1
w/o planner (uniform f)	95.46 \pm 0.4	97.68 \pm 0.3	93.86 \pm 0.6	90.24 \pm 0.3	75.62 \pm 0.7	95.34 \pm 0.3	93.42 \pm 0.3	95.78 \pm 0.3
w/o controller (i.i.d. from f)	96.72 \pm 0.3	98.68 \pm 0.2	95.42 \pm 0.5	92.04 \pm 0.2	77.36 \pm 0.6	96.68 \pm 0.2	94.86 \pm 0.2	96.98 \pm 0.2
w/o state signals ($\alpha=\beta=0$)	94.82 \pm 0.5	97.14 \pm 0.4	93.18 \pm 0.7	89.46 \pm 0.4	74.86 \pm 0.8	94.62 \pm 0.4	92.78 \pm 0.4	95.12 \pm 0.4

Table 8. **Ablation study (link prediction AUC).** Each row removes one component from ControlG. Consistent with the node classification ablation, removing the planner or both state signals causes the largest performance drops, confirming the importance of adaptive allocation and closed-loop state estimation.

state estimation rather than control.

Table 9 reports the average time per optimizer step (in milliseconds) across all methods and datasets. `ControlG` incurs modest overhead compared to simple scheduling baselines (Random, Round-Robin) due to state estimation and planning, but remains significantly faster than heavyweight multi-pretext methods such as AutoSSL and ParetoGNN. Compared to gradient-projection methods (PCGrad, CAGrad), `ControlG` achieves comparable or lower per-step cost since it avoids per-step gradient conflict resolution.

Method	Cora	CiteSeer	Chameleon	Squirrel	Actor	PubMed	Wiki-CS	Co-CS
BGRL	22.73ms	18.44ms	26.76ms	21.88ms	22.16ms	29.54ms	22.10ms	69.34ms
DGI	40.75ms	22.19ms	16.67ms	92.84ms	62.72ms	38.28ms	38.05ms	108.40ms
GRACE	42.62ms	37.66ms	29.17ms	50.05ms	73.08ms	231.40ms	111.58ms	126.68ms
MVGRL	25.99ms	14.52ms	25.68ms	—	31.67ms	15.74ms	—	74.34ms
p_link	9.78ms	10.02ms	11.62ms	12.23ms	11.15ms	13.06ms	11.94ms	18.20ms
p_recon	7.26ms	6.87ms	6.14ms	7.54ms	6.74ms	6.16ms	6.43ms	16.36ms
p_minsg	12.48ms	12.88ms	15.69ms	14.56ms	13.78ms	12.47ms	15.58ms	20.22ms
p_decor	12.02ms	13.51ms	15.56ms	15.82ms	13.12ms	15.08ms	15.90ms	20.46ms
p_par	3.43ms	8.63ms	6.38ms	5.72ms	4.79ms	3.54ms	3.39ms	9.76ms
AutoSSL	167.68ms	178.37ms	124.93ms	284.44ms	357.78ms	193.36ms	413.90ms	186.04ms
WAS	31.27ms	41.21ms	28.32ms	40.18ms	47.45ms	40.48ms	38.83ms	69.28ms
Uniform	32.24ms	36.30ms	40.15ms	38.74ms	36.21ms	46.76ms	44.71ms	95.43ms
ParetoGNN	68.69ms	34.94ms	83.57ms	70.13ms	763.93ms	80.26ms	45.03ms	203.01ms
PCGrad	35.57ms	40.37ms	47.25ms	42.19ms	44.12ms	52.81ms	49.55ms	99.00ms
CAGrad	47.85ms	45.24ms	44.31ms	54.49ms	66.42ms	62.77ms	59.83ms	104.18ms
Random	8.08ms	8.53ms	11.58ms	12.77ms	11.09ms	8.86ms	10.19ms	15.07ms
Round-Robin	8.66ms	10.91ms	10.80ms	10.64ms	11.07ms	8.82ms	11.01ms	21.93ms
<code>ControlG</code>	24.03ms	16.47ms	26.08ms	27.45ms	26.35ms	29.08ms	28.56ms	31.44ms

Table 9. Time per optimizer step (ms). Wall-clock time averaged over all training steps, measured on a single NVIDIA H200 GPU. `ControlG` adds modest overhead for state estimation and planning compared to naive scheduling (Random, Round-Robin), but is significantly faster than AutoSSL and ParetoGNN, and comparable to gradient-projection methods (PCGrad, CAGrad).

D.9. Diagnostics: scheduling, tracking, and state

We visualize the closed-loop behavior of `ControlG` via block-level traces: task selection timelines, deficit trajectories, and state trajectories (spectral demand, interference, composite difficulty). These figures are generated directly from the JSONL logs produced during training and provide transparency into how `ControlG` adapts its scheduling over the course of pretraining.

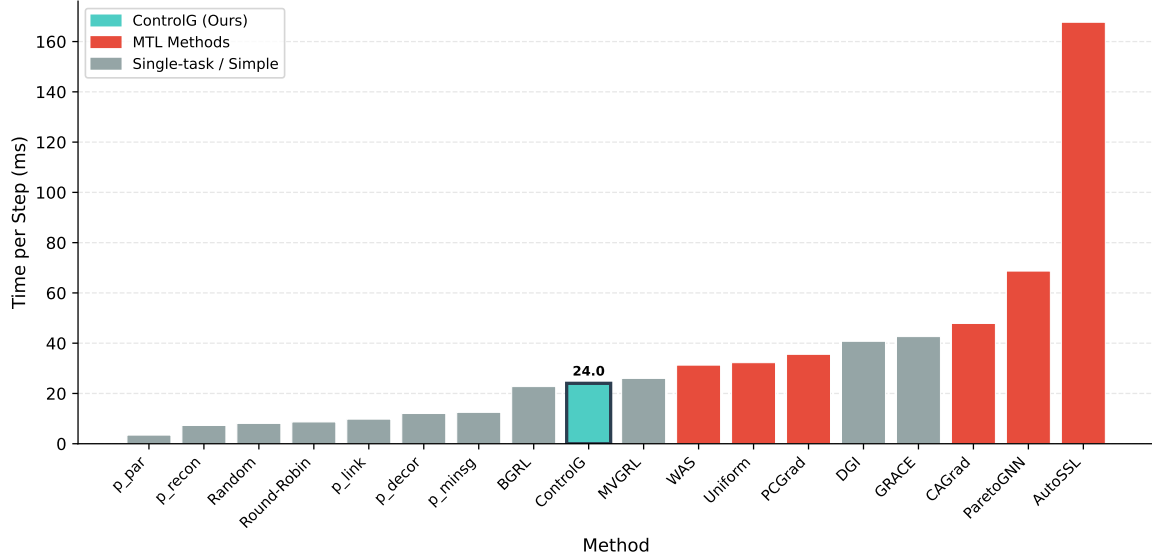


Figure 3. **Time per step on Cora.** Bar plot comparing wall-clock time (ms) per optimizer step across all methods. ControlG (highlighted in teal) incurs modest overhead compared to simple scheduling baselines (p.par, Random, Round-Robin) but is significantly faster than heavyweight methods like AutoSSL and ParetoGNN.



Figure 4. **Task scheduling timeline.** Top: Scatter plot showing which pretext task was selected at each training block (raster view). Bottom: Stacked area chart showing the running proportion of recent blocks allocated to each task. The visualization reveals how ControlG dynamically shifts focus between tasks over training—initially exploring broadly, then concentrating on tasks with higher difficulty or interference signals.

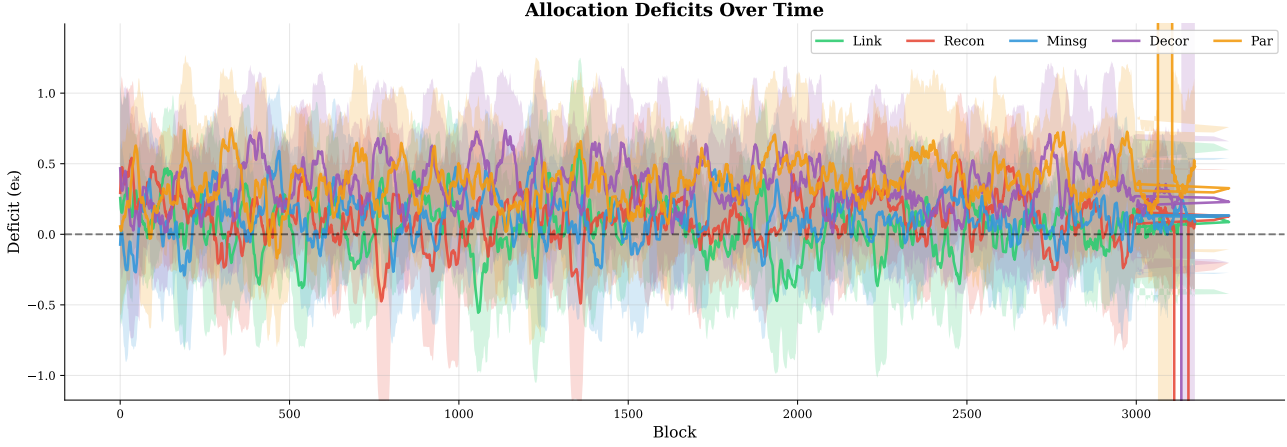


Figure 5. Allocation deficit trajectories. Deficit $e_k(t)$ for each pretext task over training blocks, showing how far each task is from its target allocation (mean \pm 1 std across seeds). Positive values indicate the task is under-scheduled relative to its target; negative values indicate over-scheduling. The PID controller drives deficits toward zero, ensuring long-run tracking of the planned allocation while allowing short-term deviations for exploration.

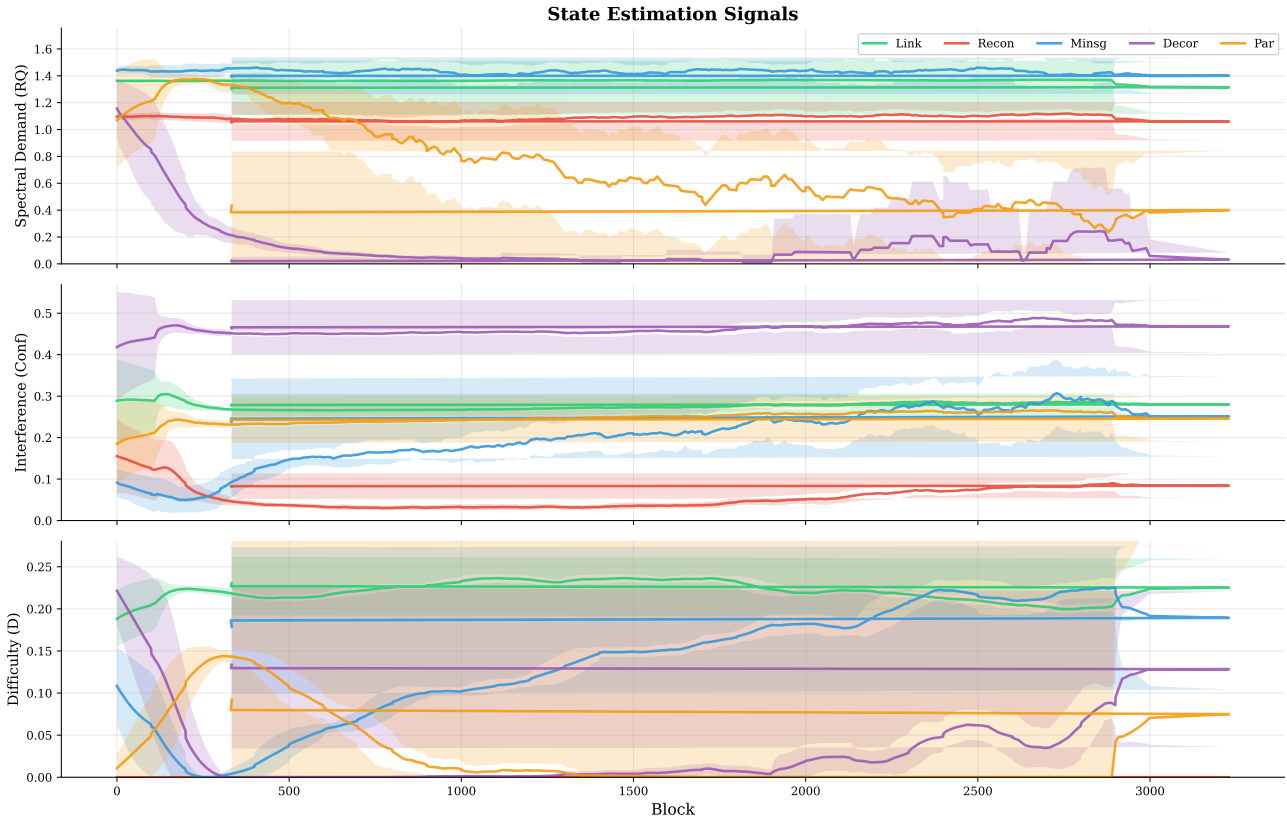


Figure 6. State estimation signals over training. *Top (RQ):* Spectral demand—gradient magnitude indicating how much each task “needs” training. *Middle (Conf):* Interference—gradient conflict between tasks, higher values suggest scheduling separately. *Bottom (D):* Composite difficulty estimate combining both signals. These sensor readings drive ControlG’s planning decisions: tasks with high difficulty receive larger allocations in the next planning window.

Algorithm 2 ControlG (detailed): sense–plan–control on the full graph

Require: Graph $G = (V, E)$ with normalized Laplacian \tilde{L} ; objectives $\{L_k\}_{k=1}^K$; encoder θ ; optimizer Opt

Require: Epochs T , batches/epoch B_{ep} , block size B_{block} , sensing period u , temperature τ , exploration ϵ

Require: Difficulty params $\alpha, \beta, \gamma, \rho, \rho_L, [D_{\min}, D_{\max}]$; PID gains K_P, K_I, K_D ; clamp I_{\max} ; margin δ ; stabilizer ε

- 1: **[CTRL]** Initialize θ ; set $D_k \leftarrow D_{\min}$, $\tilde{L}_k \leftarrow 1$, $r_k \leftarrow +\infty$ for all k *// conservative init*
- 2: **[SENSE]** **Warm-up:** run few steps per task to get L_k^{scale} , init $\tilde{L}_k \leftarrow L_k/(L_k^{\text{scale}} + \varepsilon)$, $r_k \leftarrow \tilde{L}_k + \delta$ *// scale normalization*
- 3: **for** epoch $t = 1, \dots, T$ **do**
- 4: **[CTRL]** $M \leftarrow \lceil B_{\text{ep}}/B_{\text{block}} \rceil$; reset $N_k, N_k^{\text{ref}}, I_k, e_k^{\text{prev}} \leftarrow 0$ for all k *// epoch init*
- 5: **for** block $m = 1, \dots, M$ **do**
- 6: **if** $m = 1$ or $(m - 1) \bmod u = 0$ **then**
- 7: **for** $k = 1, \dots, K$ **do**
- 8: **[SENSE]** $\ell_k \leftarrow L_k(\theta; G)$; $H_k \leftarrow \nabla_Z L_k$; $g_k \leftarrow \nabla_\theta L_k$ *// full-graph losses and gradients*
- 9: **[SENSE]** $\mathcal{E}_k \leftarrow \text{tr}(H_k^\top \mathbf{L} H_k)$; $\text{RQ}_k \leftarrow \mathcal{E}_k / (\|H_k\|_F^2 + \varepsilon)$ *// Dirichlet energy, spectral demand*
- 10: **end for**
- 11: **[SENSE]** $\hat{g}_k \leftarrow g_k / \|g_k\|_2$; $Q_{ij} \leftarrow \langle \hat{g}_i, \hat{g}_j \rangle$; solve $\lambda^* \leftarrow \arg \min_{\lambda \in \Delta^K} \frac{1}{2} \lambda^\top Q \lambda$ *// normalize, MGDA*
- 12: **for** $k = 1, \dots, K$ **do**
- 13: **[SENSE]** $c_{k,j} \leftarrow [-\cos(g_k, g_j)]_+$; $\text{Conf}_k \leftarrow \sum_{j \neq k} \lambda_j^* c_{k,j}$ *// pairwise conflict, interference score*
- 14: **end for**
- 15: **[SENSE]** $\overline{\text{RQ}}, \overline{\text{Conf}} \leftarrow \text{RobustNorm}(\text{RQ}), \text{RobustNorm}(\text{Conf})$ *// normalize across tasks*
- 16: **for** $k = 1, \dots, K$ **do**
- 17: **[SENSE]** $D_k \leftarrow \text{clip}((1 - \rho)D_k + \rho(\alpha \overline{\text{RQ}}_k + \beta \overline{\text{Conf}}_k), [D_{\min}, D_{\max}])$ *// difficulty EMA*
- 18: **[SENSE]** $\tilde{L}_k \leftarrow (1 - \rho_L)\tilde{L}_k + \rho_L \ell_k / (L_k^{\text{scale}} + \varepsilon)$ *// normalized loss EMA*
- 19: **[PLAN]** $r_k \leftarrow \max(r_k, \tilde{L}_k + \delta)$; $w_k^{\text{HV}} \leftarrow 1 / (r_k - \tilde{L}_k + \varepsilon)$; $a_k \leftarrow w_k^{\text{HV}} / (1 + \gamma D_k)$ *// HV sens., priority*
- 20: **end for**
- 21: **[PLAN]** $f_k \leftarrow a_k / \sum_j a_j$ for all k *// allocation plan*
- 22: **end if**
- 23: **for** $k = 1, \dots, K$ **do**
- 24: **[CTRL]** $N_k^{\text{ref}} \leftarrow N_k^{\text{ref}} + f_k$; $e_k \leftarrow N_k^{\text{ref}} - N_k$; $I_k \leftarrow \text{clip}(I_k + e_k, [-I_{\max}, I_{\max}])$ *// deficit, integral*
- 25: **[CTRL]** $\Delta e_k \leftarrow e_k - e_k^{\text{prev}}$; $\nu_k \leftarrow K_P e_k + K_I I_k + K_D \Delta e_k$ *// PID logits*
- 26: **end for**
- 27: **[CTRL]** $p \leftarrow (1 - \epsilon) \text{softmax}(\nu / \tau) + \frac{\epsilon}{K} \mathbf{1}$; sample $k_{t,m} \sim \text{Cat}(p)$ *// stochastic policy*
- 28: **for** $j = 1, \dots, B_{\text{block}}$ **do**
- 29: **[CTRL]** $\theta \leftarrow \text{Opt}(\theta, \nabla_\theta L_{k_{t,m}}(\theta; \xi_{t,m,j}))$ *// single-task block update*
- 30: **end for**
- 31: **[CTRL]** $N_{k_{t,m}} \leftarrow N_{k_{t,m}} + 1$; $e_k^{\text{prev}} \leftarrow e_k$ for all k *// update counts and memory*
- 32: **end for**
- 33: **end for**
